SANDIA REPORT

SAND2008-7934
Unlimited Release
Printed December 2008

A Dual Neutron/Gamma Source for the Fissmat Inspection for Nuclear Detection (FIND) System

Arlyn Antolak, Barney Doyle, Michael King, Floyd McDaniel,
Daniel Morse, Paula Provencio, Tom Raber, Paolo Rossi

Prepared by
Sandia National Laboratories
Albuquerque, New Mexico 87185 and Livermore, California 94550

Sandia is a multiprogram laboratory operated by Sandia Corporation,
a Lockheed Martin Company, for the United States Department of Energy's
National Nuclear Security Administration under Contract DE-AC04-94AL85000.

Issued by Sandia National Laboratories, operated for the United States Department of Energy by Sandia Corporation.

Available to DOE and DOE contractors from
U.S. Department of Energy
Office of Scientific and Technical Information
P.O. Box 62
Oak Ridge, TN 37831

Telephone: (865)576-8401
Facsimile: (865)576-5728
E-Mail: reports@adonis.osti.gov
Online ordering: http://www.osti.gov/bridge

Available to the public from
U.S. Department of Commerce
National Technical Information Service
5285 Port Royal Rd
Springfield, VA 22161

Telephone: (800)553-6847
Facsimile: (703)605-6900
E-Mail: orders@ntis.fedworld.gov
Online order: http://www.ntis.gov/help/ordermethods.asp?loc=7-4-0#online

SAND2008-7934
Unlimited Release
Printed December 2008

A Dual Neutron/Gamma Source for the Fissmat Inspection for Nuclear Detection (FIND) System

Arlyn Antolak, Daniel Morse, Tom Raber, Michael King
Engineered Materials Department
Sandia National Laboratories
P.O. Box 969
Livermore, CA 94551

Barney Doyle, Floyd McDaniel, Paolo Rossi, Paula Provencio
Radiation-Solids Interactions Department
Sandia National Laboratories
P.O. Box 5800
Albuquerque, New Mexico 87185

Abstract

Shielded special nuclear material (SNM) is very difficult to detect and new technologies are needed to clear alarms and verify the presence of SNM. High-energy photons and neutrons can be used to actively interrogate for heavily shielded SNM, such as highly enriched uranium (HEU), since neutrons can penetrate gamma-ray shielding and gamma-rays can penetrate neutron shielding. Both source particles then induce unique detectable signals from fission. In this LDRD, we explored a new type of interrogation source that uses low-energy proton- or deuteron-induced nuclear reactions to generate high fluxes of mono-energetic gammas or neutrons. Accelerator-based experiments, computational studies, and prototype source tests were performed to obtain a better understanding of 1) the flux requirements, 2) fission-induced signals, background, and interferences, and 3) operational performance of the source. The results of this research led to the development and testing of an axial-type gamma tube source and the design/construction of a high power coaxial-type gamma generator based on the $^{11}B(p,\gamma)^{12}C$ nuclear reaction.

CONTENTS

FIGURES

TABLES

Preface

This report describes an LDRD project titled "A Dual Neutron/Gamma Source for the Fissmat Inspection for Nuclear Detection (FIND) System" (LDRD project #95367). The report is divided into the following chapters:

- **Chapter 1** is an introduction to active interrogation and describes the problem.
- **Chapter 2** describes the physics of neutron-producing, monoenergetic gamma-producing, and mixed particle-producing nuclear reactions.
- **Chapter 3** describes thermal load experiments and microscopic analysis to evaluate candidate (p,γ) and (d,n) target materials
- **Chapter 4** describes low-energy (< 700 keV) ion accelerator experiments and results that were used to evaluate the source configurations and operational parameters.
- **Chapter 5** describes high-energy (> 1 MeV) ion accelerator experiments and results that were used to evaluate the source configurations and operational parameters.
- **Chapter 6** describes experimental investigations to determine the cross section of alternative low-energy neutron-producing reactions.
- **Chapter 7** describes the development and evaluation of prototype nuclear reaction-based monoenergetic gamma sources.
- **Chapter 8** describes computational models and results that were used to predict the performance of the source for active interrogation.
- **Chapter 9 s**ummarizes experimental and computational results.
- **Chapter 10** lists references cited in the report.

Executive Summary

Detecting heavily shielded special nuclear material, especially highly enriched uranium, is very challenging problem. Passive radiation detection, high-energy radiography, and manual (visual) inspections can be used to screen suspicious objects, but each of these inspection techniques has some limitations. Passive detection is difficult because the natural decay from even large amounts of nuclear material can be shielded or masked by materials with higher than normal background radiation. Radiography can identify objects containing high density materials, but a two-dimensional projected density images have difficulty distinguishing small volumes of nuclear material surrounded by thick shielding. Visual inspection of suspicious cargo is impractical on a large scale because of the expense in terms of manpower and delays to commerce. Active interrogation, using high-energy neutrons and photons to stimulate fission-induced neutron and gamma-ray signals, provides an unambiguous signature of fissile material. However, the practical use of active interrogation systems has been limited due to the imposed administrative restrictions on both the energy and dose of the interrogating radiation to minimize activation of or damage to surrounding materials/objects. Intentional shielding used to attenuate either the interrogation source beam or the emitted fission-induced signals will also increase the requirements of the radiation source. Because neutrons are more efficiently shielded by hydrogeneous materials and photons by higher atomic number materials, an active interrogation screening system should include both particle types.

This report describes a three-year research and development program investigating the fundamental engineering physics and material science needed to develop such a dual-particle interrogation source. The source exploits low-energy proton- and deuteron-induced nuclear reactions to generate high fluxes of mono-energetic gammas and/or neutrons. The use of low-energy reactions allows the source to be simpler in design, more cost effective, more efficient, and easier to scale than comparable high-energy particle accelerator alternatives. Additionally, in the case of the gamma source, active interrogation with mono-energetic photons results in significantly lower radiation dose to surroundings and system operators. We assessed the viability of this source for interrogation through a program of experiments and simulations that determined the performance limits of a field-deployable system. The results obtained from this LDRD project led to the procurement of outside funding to 1) develop and test a prototype axial-type 12-MeV mono-energetic gamma tube source and 2) design/construct a prototype high power coaxial-type 12-MeV mono-energetic gamma generator based on the $^{11}B(p,\gamma)^{12}C$ nuclear reaction.

1. INTRODUCTION

Each year approximately 6 million maritime cargo containers are delivered to U.S. ports. Due to the size and complexity of their cargo, these containers offer a variety of opportunities for smuggling different kinds of contraband, including the possibility of a nuclear weapon or the components to assemble one. Failure to detect a concealed nuclear weapon or improvised nuclear device would lead to major physical damage and loss of life in an urban center as well as major economic and psychological damage throughout the entire U.S. At present, only a small fraction of containers are inspected beyond a routine document screening, although passive detection and radiographic imaging systems are becoming more commonplace at the nation's largest ports. The drawback to passive inspection is that the natural radioactive emissions from fissile materials can be shielded fairly easily (e.g., by the surrounding cargo or intentionally emplaced shielding) or are difficult to detect (due to background, short collection times, and poor detected signal statistics). A more reliable approach is to actively interrogate for the nuclear material with high-energy neutrons and/or photons to induce fission signals (neutrons and gamma-rays) that can be detected after penetrating through cargo or other shielding materials. In particular, an interrogation source capable of producing *both* neutrons and photons is optimal because neutrons readily penetrate photon absorbing media (e.g., higher atomic number or dense materials), while photons are useful for hydrogeneous or neutron absorbing types of materials.

An intense interrogation system will have high detection probability and a low false alarm rate so that reliable screenings can be completed with minimal inspection time. However, producing such high-intensity sources for active interrogation has typically required using large accelerator systems such as RFQs (radio frequency quadrupoles) and linacs (linear accelerators). Less intense, but more compact, radiation sources include simple D-D or D-T tubes that use fusion processes and some particle generators based on (p, n), (D, n) or (p, γ) nuclear reactions. In this LDRD project, we explored the underlying physics and requirements of a new interrogation source that uses low-energy proton- or deuteron-induced nuclear reactions to generate high fluxes of mono-energetic gammas or neutrons. The use of low-energy reactions allows the source to be simpler in design, more cost effective, more efficient, and easier to scale than comparable high-energy particle accelerator alternatives. Additionally, the use of mono-energetic gammas results in lower radiation doses to both the surroundings and system operators. We assessed the viability of this source through a program of experiments and simulations that determined the performance limits of a field-deployable interrogation system. Our research approach involved 1) establishing the scientific basis and underlying materials science required in the design of the source and associated (p,γ) reaction targets, 2) performing analyses to evaluate configurations and operational parameters for the system, and 3) validating the simulation model results by comparing to experimental measurements on ion accelerators. The results of the experiments and simulations were eventually used to define the parameter space over which this interrogation technology, which we call the FIND (Fissmat Inspection for Nuclear Detection) system, is feasible.

2. NUCLEAR REACTIONS

The FIND interrogation source uses low-energy nuclear reactions to produce high-energy neutron beams, gamma beams, or mixed particle (neutron/gamma) beams. Nuclear reactions require a stable or long-lived target nucleus (e.g., d, t, He, Li, Be, B, C, N, O, F) for the target and an incident particle beam (e.g., p, d, ^{3}He, α) that can be easily produced and accelerated to an energy at which the reaction can occur. In order to induce fission in SNM, photon energies need to be greater than the photofission threshold energy which is approximately 5.5 MeV for fissile materials. Neutrons, on the other hand, can induce fission down to thermal energies (0.025 eV) but require high (megavolt) energies to increase penetration depths. The next sections discuss low-energy (<500 keV) reactions that can produce gammas and neutrons by compact interrogation sources.

2.1. Neutron-Producing Nuclear Reactions

The d-t reaction, ^{3}H(d,n)^{4}He, is a well-known and very efficient reaction for producing 14-MeV neutrons. This reaction has a Q-value of 17.6-MeV, with the remaining 3.6-MeV going to the helium nucleus. The reaction cross section peaks around 100 kV (~5 b), so this is the energy where typical commercial generators operate. The 14-MeV d-t neutrons can effectively penetrate through thick shielding and induce fission in SNM. On the other hand, the handling and supply of tritium as well as neutron activation are concerns for these systems if they are to be deployed in the field.

The ^{2}H(d,n)^{3}He, or "d-d", reaction has moderate strength and produces 2.5 MeV neutrons. The cross section has a broad peak (~100 mb) around 2.5 MeV and, for comparison, the cross section at 100 kV deuteron energy is approximately two orders of magnitude times smaller than the d-t cross section. For energies above 100 kV, a forward directed and higher energy neutron beam can be produced with the d-d reaction because of the kinematics.

Proton- and deuteron-induced nuclear reactions are also routinely used to make beams of neutrons for nuclear physics experiments. The ^{6}Li(d,n)^{7}Be reaction (producing 2.7-MeV neutrons) and the ^{7}Li(d,n)^{8}Be reaction (producing 13-MeV neutrons) both have a cross section of ~50 mb at 300 kV which is comparable to the d-d cross section at that energy. Similarly, the ^{9}Be(d,n)^{10}B reaction at 500kV (producing 1-4 MeV neutrons) has a cross section of approximately 80 mb. Directional neutron beams based on near threshold ^{7}Li(p,n)^{7}Be reaction with proton beam energies between 1.882 MeV to 1.92 MeV have been considered for boron neutron capture therapy (BNCT) in medical applications. The threshold proton energy of the reaction is 1.88-MeV requiring a larger accelerator and the generated neutron energies are low (50 – 100 keV) so that they are easily shielded from reaching the SNM material.

2.2. Monoenergetic Gamma-Producing Nuclear Reactions

Over 500 nuclear reactions have been identified that produce monoenergetic gammas with energies greater than the photofission threshold (5.5 MeV). However, the vast majority of these reactions do not generate "pure" photon beams; instead they produce mixed particle beams of photons and neutrons (or other particles). For example,

deuteron-induced reactions are threshold-type reactions that produce a combination of high-energy gammas and high fluxes of neutrons. If higher mass incident particles (^{3}He, α, etc.) are used, then the channel for producing gammas becomes weaker in preference to generating other particles, such as neutrons.

At low energies, many proton-induced reactions occur as narrow resonances and generally only produce monoenergetic gammas (see Table 1). Nature's lowest energy nuclear reaction, $^{11}B(p,\gamma)^{12}C$, produces three gamma-rays at 4.4/11.7 MeV (97% emission fraction) and 16.1 MeV (3% emission fraction) of which the latter two are useful for inducing photofission (the peak of photofission cross section is approximately14-MeV). In addition, data in the literature have shown that the 11.7-MeV gamma intensity exhibits some enhanced forward directionality (~20% enhancement). The main limitation of the $^{11}B(p,\gamma)^{12}C$ reaction is its low cross section (0.16 mb) and fairly narrow resonance width (7 kV).

The $^{19}F(p,\gamma)^{16}O$ reaction produces a 6.1-MeV gamma which, unfortunately, is only slightly above the photofission threshold. On the other hand, intense gamma beams can be generated by this reaction since most of the low-energy resonances give large cross sections (>30mb). The $^{7}Li(p,\gamma)^{8}Be$ reaction at 441 kV resonance energy also has a fairly large cross section and it produces two gammas that are both close to the peak of the photofission cross section.

TABLE 1. Low-energy nuclear reaction resonances suitable for generating monoenergetic gamma-rays. The main gammas used to induce photofission are highlighted in boldface.

Reaction	E_γ (MeV)	E_p (keV)	σ (mb)	Γ (keV)	Target
$^{11}B(p,\gamma)^{12}C$	4.4, **11.7**, 16.1	163	0.16	7	Easy
$^{11}B(p,\gamma)^{12}C$	4.4, **12.2**	675	0.05	322	Easy
$^{13}C(p,\gamma)^{14}N$	4.11, **8.06**	550	1.44	33	Moderate
$^{19}F(p,\alpha\gamma)^{16}O$	**6.1**, 6.9, 7.1	340 484 597 672	160 32 7 57	3 1 30 6	Difficult
$^{19}F(p,\alpha\gamma)^{16}O$	1.6, **11.9**	672	0.5	6	Difficult
$^{7}Li(p,\gamma)^{8}Be$	**14.8, 17.7**	441	6	12	Moderate

2.3. Mixed Particle-Producing Nuclear Reactions

Nuclear reactions induced by deuterons produce mixed particle gamma/neutron beams for interrogation. For example, the $^{11}B(d,n\gamma)^{12}C$ reaction has a threshold energy of 2-MeV and produces a set of intense 4.4 and 15.1 MeV gammas and less intense gammas at 10.7 and 12.7 MeV. It also produces neutrons having an energy spectrum that peaks around 12

MeV with a broad distribution at lower energies. Similarly, the $^{7}Li(d,n\gamma)^{8}Be$ reaction requires at least 360 keV deuterons to produce a mixed beam of 17 MeV gammas and 13 MeV neutrons. The $^{7}Li(d,n\gamma)^{8}Be$ reaction is particularly intriguing for use in compact neutron/gamma sources because a very intense gamma beam can be produced with only modest beam current (only ~40 mA beam current is needed to generate $>10^{10}$ γ/s with 365 keV deuterons). An intense neutron source could also be developed because of its large cross section above 300 keV.

TABLE 2. Representative deuteron-induced nuclear reactions for generating mixed particle beams of megavolt-energy neutrons and monoenergetic gamma-rays.

Reaction	E_γ (MeV)	E_n	Cross Section
$^{11}B(d,n\gamma)^{12}C$	4.4, 10.7, 12.7, 15.1	12 MeV; broad low-energy distribution	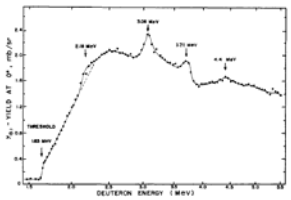 (from H-.M. Kuan *et al.,* Nuclear Physics 60 (1964) 509)
$^{6}Li(d,p\gamma)^{12}C$ $^{6}Li(d,n\gamma)^{12}C$	0.429 0.478	2.5-2.9 MeV	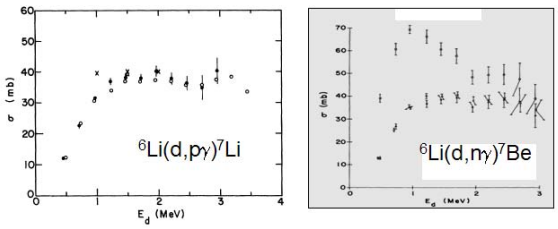 (from C.R. McClenahan *et al.,* Phys. Rev. C 11(2) (1975) 370)
$^{7}Li(d,n\gamma)^{12}C$	12.2, 13.9, 14.5, 15.3, 17.0	13.3 MeV	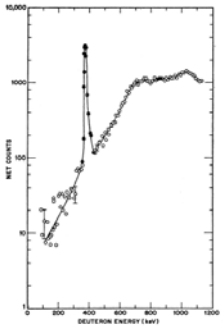 (from W.L. Imhof *et al.,* Phys. Rev. 139(4B) (1963) B904)

3. TARGET MATERIALS

The FIND source is based on using low-energy nuclear reactions to produce high-energy particles for interrogation, i.e., "nature's (nuclear) amplification". Because of the high power density on the target, is important that it has sufficient thermal conductivity to prevent overheating and beam damage. The target material should also have sufficient electrical conductivity to prevent charging that could significantly reduce the energy of the incoming protons. If the material is a compound, the other constituents should have low atomic number to maximize the proton range and, therefore, the production of gamma-rays. It must also be mechanically stable to resist cracking or crumbling after long irradiations and be reasonably easy to fabricate (either by machining or coating on a suitable substrate). Finally, the target material should contain a high concentration of the desired isotope in the nuclear reaction.

3.1. Candidate Materials

A survey was made for candidate target materials for these nuclear reactions and several compounds were identified that possess the above material properties. Both lanthanum hexaboride (LaB_6) and boron carbide (B_4C) had suitable properties for a gamma source using the $^{11}B(p,\gamma)$ reaction (see Table 1). LaB_6 is a rigid ceramic with good thermal shock resistance and good chemical and oxidation resistance. Additionally, it has high electron emissivity and good electrical conductivity which is why it is commonly used as a cathode material in electron microscopes. We obtained both bulk and coated samples of LaB_6 for testing. Similarly, boron carbide is one of the hardest materials known, ranking third behind diamond and cubic boron nitride. It has very good chemical resistance, good nuclear properties (e.g., it is used as a neutron absorber in reactors), and has low density (2.52 g/cm3). B_4C can be formed as a coating on a suitable substrate by vapor phase reaction techniques using boron halides or di-borane with methane or another chemical carbon source. Boron carbide has very similar physical properties to LaB_6 although its thermal conductivity is lower (1 Ohm-cm compared to 27 μOhm-cm for LaB_6). On the other hand, the calculated voltage drop across a 1 cm thickness of B_4C, even when exposed to a (peak) proton current density of 1 A/cm^2, would only be 1 volt.

For the fluorine and lithium nuclear reactions listed in Table 1, lithium fluoride (LiF) and calcium fluoride (CaF_2) were identified as candidate target materials. Kvamme *et al.* report[1] LiF as having a cubic rock salt crystal structure with melting temperature of 1140 ^{o}K (870°C), thermal conductivity of 14.2 W/(m K), and density of 2.6 g/cm^3. Lithium fluoride is most widely used as a flux in the production of ceramics, such as enamels, glasses and glazes. LiF is attacked by atmospheric moisture at 400°C and softens at 600°C, and it is sensitive to thermal shock and irradiation.[1, 2] CaF_2 is a cubic fluorite crystal structure with a melting point of 1360°C, density of 3.18 g/cm^3, thermal conductivity 10.0 W/(m K). Lithia (Li_2O, cubic fluorite crystal structure) was also tested because it has a high melting temperature, 1700°C, and it was thought that this would be desirable for a lithium-only target (i.e., the production of fluorine gamma-rays occurs at lower incident energy than the lithium reaction). Li_2O is used as a flux in production of batteries. The main drawback to Li_2O is that it is a severe respiratory irritant, is sensitive

to CO_2 and moisture in air and it readily captures hydroxyl groups and forms a hydroxide.[3]

3.2. Sample Preparation

Thin films of target materials were prepared by evaporation. Since the width of the resonance for the $^{7}Li(p,\gamma)^{8}Be$ nuclear reaction is ~12 keV, the thicknesses of the LiF and Li films used in the present tests were about two times the thickness given by the resonance width for a 441 keV energy proton (~3000 Å). For the CaF_2 film, the width of the $^{19}F(p,\gamma)^{16}O$ nuclear reaction is ~3 keV. The film thickness evaporated in this case was about three times the thickness given by the resonance width for a 340 keV energy proton (or ~1000 Å). $LiNbO_3$ sample was a transparent green single crystal. The boron-containing samples consisted of bulk polycrystalline LaB_6 and a B_4C block.

3.3. Rapid Thermal Load Experiments

In order to test Li and F containing materials for thermal stability, LiF, Li, CaF_2, and Li_2O were grown in various configurations on Cu substrates and heated in argon (Ar) or vacuum. In a rapid thermal furnace, samples designated as LiF/Cu, LiF/Cr/Cu, and CaF_2/Li/Cu were heated for 15 minutes (time limited to furnace) on a Si wafer holder and under a flowing Ar atmosphere. The samples were made as follows: "LiF/Cu" was 3000 Å LiF on thick Cu disk, "LiF/Cr/Cu" was 3000 Å LiF on Cr buffer layer on thick Cu disk, and "CaF_2/Li/Cu" was 3000 Å Li on 1000 Å CaF_2 on thick Cu disk. At temperatures of 300°C, 500°C, and 700°C, the samples were kept at the actual temperature for at least 15 minutes. A fourth thermal test in argon heated the sample to 900°C, but the furnace automatically shut off after being at 900°C for 10 minutes. The shutoff may have occurred due to a failure in the argon flow since the samples were mostly covered in a grey coating.

In a second rapid thermal test, five LiF/Cu-thin (3000 Å LiF on thin polished/etched Cu TEM disks) were subjected to separate rapid thermal tests in a vacuum furnace at approximately 10^{-6} torr. Three samples were heated for an hour at 600°C, 800°C, or 1000°C. A fourth sample that had been at 700°C for an hour was reheated for another hour at 1000°C. A fifth sample was kept at room temperature.

The third rapid thermal test was on six sample disks of CaF_2/ Li_2O/Cu-thin (3000 Å CaF_2 on 3000 Å Li_2O on thin polished/etched Cu TEM disks). Samples were subjected to separate rapid thermal tests in a vacuum chamber at approximately 10^{-6} torr. One sample was heated for an hour at 600°C and another at 800°C. Two samples were heated at 1000°C while two samples were kept at room temperature.

3.4. Electron Beam Heating Experiments

Four samples were selected for electron beam (ebeam) testing: crystalline LaB_6, single crystal $LiNbO_3$, polycrystalline B_4C block, and LiF/Cr on thick Cu disk which had previously been heated to 700°C was subsequently electron beam heated to 1000°C. Each sample was heated using a 4 kV electron beam evaporator. The temperature was monitored using a Mikron M190 pyrometer. The samples were heated until some form of damage was observed. LiF was ebeam heated just below the melting temperature of

Cu. The actual temperature reading of the pyrometer was 972°C, but the pyrometer emissivity could only be set as low as 0.1 and should have been lower for LiF (this would have raised the temperature reading). Thus, the estimated temperature was 1000°C.

3.5. Rapid Thermal Load Tests in Argon

Table 2 shows the sample materials used for the thermal tests, the temperature and environment the samples were exposed to, and a short description of observations from the tests. The first series of rapid thermal tests on LiF/Cu, LiF/Cr/Cu, and CaF_2/Li/Cu samples were done in flowing argon. After the 300°C and 500°C rapid thermal tests, optical microscopy (OM) and scanning electron microscopy (SEM) showed that the morphology of the samples was unchanged. For the LiF/Cr/Cu sample, its original blue color faded to a light green indicating a color center change had occurred during heating.

TABLE 2. Summary of the samples, thermal test environments, and results

Material: Film/on Cu or Crystal	Ebeam Heating°C	Ebeam Power W	Furnace Heating°C	Furnace Heating	Results: SEM,EDS (F peak), or observation by eye
LiF/Cr/Cu			700	Ar	Crystalline film, strong F
LiF/Cr/Cu			900	Ar	Crystalline film, small holes, weakened F
CaF/Li/Cu			700	Ar	Mixed morphology, weak F
LiF/Cu	1000	40	700	Ar	1st furnace heat: Crystalline film, weak F 2nd ebeam: Crater in crystalline film, no F
LiF/Cu			800	Vac	Crystalline film, very weak F
LiF/Cu			1000	Vac	Crystalline film, small holes, no F
Li_2O/Cu			800	Vac	Crystalline film, some etched Cu
Li_2O/Cu			1000	Vac	Crystalline film, very etched Cu
$LiNbO_3$	1170	88			Melted
LaB_6	1860	360			Slight roughened crystalline surface
B_4C	unk	76			Crystal broke violently on power load

The samples were then heated to 700°C in flowing argon. OM of the samples showed some changes in morphology. In particular, SEM showed both LiF/Cu and LiF/Cr/Cu samples had some thin facet edges indicative of crystallization. Figure 1 shows SEM micrographs that compare the surface morphologies of the LiF/Cr/Cu and LiF/Cu . The LiF/Cu which had no buffer layer shows some cracking and small holes. The LiF/Cr/Cu with buffer layer appeared to be more continuous with fewer micron-size holes. Energy dispersive spectroscopy (EDS) of a cross-section of LiF/Cr/Cu showed that the Cr diffused into the Cu substrate. Michaelsen *et al.* previously showed some Cu-Cr solution at very small percentage chromium.[4] Transmission electron microscopy (TEM) of the LiF/Cr/Cu cross-section showed that there were voids at the Cr-rich Cu-LiF interface and

some pits in the LiF film. EDS showed a strong fluorine peak in the LiF/Cr/Cu film. In contrast, the CaF_2/Li/Cu surface had phase-separated after 700°C and small crystals dominated the surface.

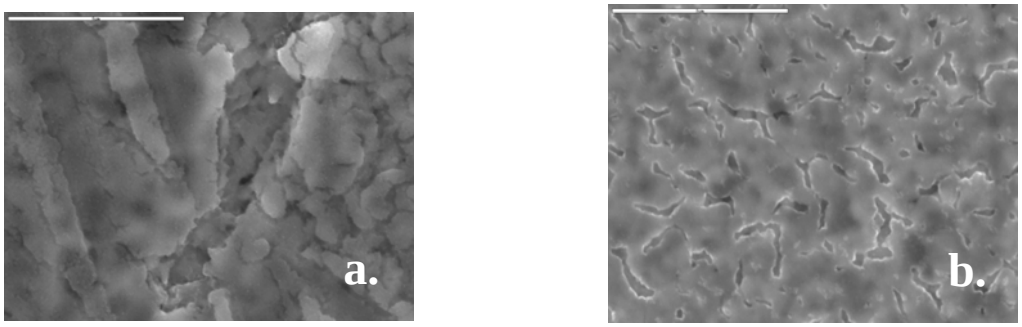

FIGURE 1. Scanning electron micrographs showing the morphologies of (a) LiF on Cr/Cu and (b) LiF on Cu after thermal load tests. The white bar is 5 microns. Micrograph "a", shows the surface after heating to 700°C in argon. After storing the sample one month in air, fluorine could be detected with energy dispersive spectroscopy (EDS). The LiF/Cu sample in micrograph "b" was also heated to 700°C in argon.

The LiF/Cu, LiF/Cr/Cu, and CaF_2/Li/Cu samples were coated with copper oxide after the 900°C thermal test. EDS showed that the coating contained copper and weak fluorine in some areas. In addition, some of the fluorine appeared to be mixed into the coating. EDS of the LiF/Cr/Cu following 900°C thermal loading showed a decrease in fluorine content compared to the 700°C sample. On the other hand, EDS of LiF/Cu with no chromium buffer layer showed that fluorine was nearly gone after the 700°C thermal test and no fluorine was detected after the 900°C thermal test (due to copper fluoridation).[5]

3.6. Rapid Thermal Load Tests in Vacuum

Five thin polished/etched copper disks were coated with 3000 Å LiF (sample designated as LiF/Cu-thin) and heated in vacuum to various temperatures above 500°C. After the 600°C rapid thermal test in vacuum, SEM of the LiF/Cu-thin sample showed the film had small regions where crystallization was taking place, while EDS quantified a weak fluorine peak. SEM the sample after an 800°C thermal test in vacuum showed a continuous film, but some small (micron-size) holes were observed. EDS showed no, or very little, amount of fluorine present. After the 1000°C thermal test, SEM showed a crystallized (possibly lithium oxide) film on the surface with abundant facets and small micron-size holes. EDS showed this film had no fluorine, so copper fluoridation was probable. The holes in the film could be caused by pitting in the copper substrate. Cross-section TEM and EDS of as-grown LiF/Cu-thin and 1000°C tested samples indicate the fluorine is being removed from the LiF film. Previously, EDS showed that the as-grown LiF/Cu-thin sample contained fluorine but, after time, it was lost. Figure 2 shows SEM micrographs of a LiF/Cu-thin on a copper TEM disk compared to a bare Cu surface after heating them to 1000°C in vacuum.

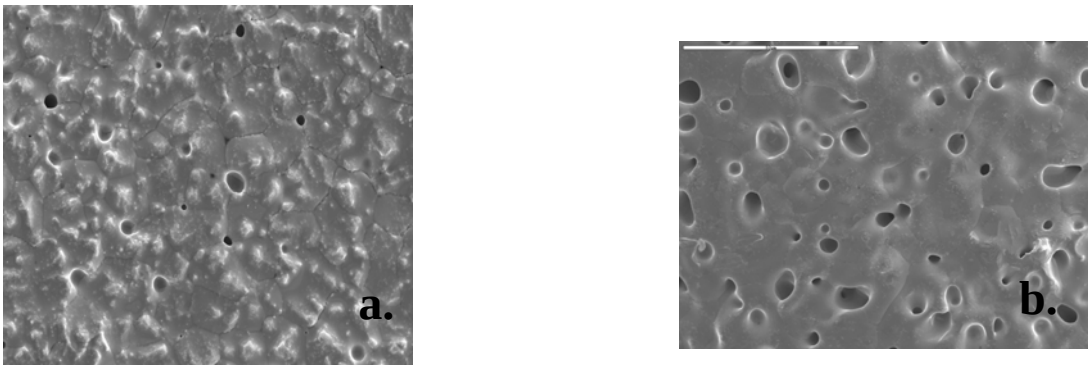

FIGURE 2. Micrographs of a.) CaF_2/Li_2O/Cu-thin sample compared to b.) bare Cu after heating to 1000°C in vacuum. The white bar is 5 microns.

An additional rapid thermal test was performed on a "CaF_2/Li_2O/Cu-thin" sample which consisted of a 3000 Å CaF_2 layer on 3000 Å Li_2O on a thin polished/etched copper TEM disk. Samples were grown in a two-layer configuration with a film of 3000 Å of Li_2O on the Cu TEM disk covered by a surface layer of 3000 Å CaF_2 to protect the Li_2O from air. SEM of the 600°C CaF_2/Li_2O/Cu-thin sample showed that abundant small crystals had grown. The crystals were small single crystals that did not form continuous films. EDS showed a weak fluorine peak. X-ray diffraction during heating showed that the broad fluoride peak disappeared between 700°C and 800°C. Above 800°C, etching of the copper substrate took place. SEM showed more abundant crystals and holes on the surface and EDS detected that very weak fluorine was present. After 1000°C heating, the copper was etched to half of its original size. A second 1000°C sample which was very thin was observed to roll up. On the backside of this sample, the bare copper surface had abundant holes and pits as shown in Fig. 2b. EDS of the 1000°C sample did not detect fluorine so the CaF_2 had also degraded. The lithia (Li_2O) pressed powder used to grow the Li_2O film was unstable under the electron beam leading to the formation of hydroxyl groups that might explain the drastic etching of the copper disks.

A 3000 Å thick layer of LiF was grown on a 200 Å film of Au on a thin Cu disk (sample designated as LiF/Au/Cu) using electron beam evaporation. The LiF/Au/Cu sample was placed in a vacuum chamber coupled to an X-ray diffraction (XRD) system. XRD at room temperature showed that the main LiF peak was very weak. No other peaks were observed indicating that the as-grown LiF/Au/Cu is amorphous or nano-crystalline in structure. During the heating of the sample at 700°C, the LiF peak sharpened slightly and a very weak peak corresponding to lithium metal started to form. Heating was continued to 850°C at which point the lithium metal peak was very strong and the LiF peak was no longer present. Electron diffraction had previously been done on FIB cut cross-sections of LiF/Cr/Cu samples one heated to 700°C in argon and one heated to 900°C in argon. The 700°C sample had diffraction spots and rings that match XRD powder files for LiF and weakly for lithium hydroxide (or possibly Li_2O). It is possible that some lithium metal also exists on this sample. The 900°C sample had areas that match lithium metal and lithium hydroxide. EDS showed the presence of fluorine after 700°C, but no fluorine was observed after 800°C.

3.7. Electron-Beam Heating Tests

Several crystalline lithium- and boron-containing materials were heated with a 4 keV electron beam (ebeam). A clear green single crystal of $LiNbO_3$ (melting temperature: 1257°C) was obtained and tested. For temperatures less than 600°C, no color center change was observed (see Ref. 6). At 20-21 mA and 80W ebeam operation, the temperature of the $LiNbO_3$ crystal rose to between 1160-1170°C which caused it to melt. LiF/Cu (on thick Cu) was also tested to a temperature of 972°C. Observation by eye showed significant discoloration of the film. SEM showed an approximately 50 micron crater in the film and no fluorine was detected by EDS. LiF is known to be very sensitive to electron irradiation which can cause fluorine to be driven off with the formation of lithium metal in vacuum.

Crystalline LaB_6 was also exposed to the ebeam and heated by slowly increasing the current. At 80 mA and 360W, the sample reached a temperature of ~1850°C but the ebeam current became unstable and the test was stopped. No ebeam damage was observed on the sample except for a slight discoloration of the purple crystalline surface. SEM showed that the polycrystalline facets had been roughened. A test was begun using a B_4C sample but just as the sample reached a temperature to cause an orange glow it violently broke into two pieces and no further experiments were performed.

3.8. Target Material Results

We found that both LaB_6 and B_4C are leading candidate materials for boron-containing targets using the $^{11}B(p,\gamma)$ reaction. No ebeam damage was observed on LaB_6 samples except for a slight discoloration of the purple crystalline surface and that the polycrystalline facets had been roughened. A B_4C sample was also ebeam heated, but the test results are inconclusive because just as the sample reached a temperature to cause an orange glow, it violently broke into pieces.

We also found that LiF and CaF_2 are potential candidates for lithium- and fluorine-containing targets, but some material issues still need to be resolved. If a suitable buffer layer for the Cu substrate is found, it is possible more robust LiF and CaF_2 films could result. However, LiF has a poor ability to resist thermal shock and electron beam irradiation so CaF_2 may be better in that regard. While CaF_2 may be more thermal shock resistant and have a higher melting temperature than LiF, our rapid thermal test results showed that CaF_2 formed a non-uniform, discontinuous morphology with low fluorine content. A buffer layer on Cu surface may reduce the loss of fluorine. If high quality LiF on Cu is used for a target material, the temperature of the target could be kept below 850°C by spreading the incident beam out to reduce the power density on target. In addition, if the Cu substrate were cooled it may be possible to keep the temperature low enough. Other Li-containing materials that should be tested are Li_4SiO_4, Li_2SiO_3, Li_2TiO_3, Li_2WO_4, or Li_2ZrO_3. Compounds a=such as Li_2O, also known as lithia, have a higher melting temperature than LiF and probably handles thermal shock better, but it is difficult to keep from forming a hydroxide which attacks Cu. Some of the more complex compounds such as $LiNbO_3$ do not appear to be good candidates for the lithium-containing target material.

4. LOW-ENERGY ACCELERATOR EXPERIMENTS

The photofission cross section for most nuclear materials has a peak that extends from approximately 5-MeV to 20-MeV. In particular, the peak for ^{235}U is at 13.8-MeV with a full-width-at-half-maximum of 5-MeV and a threshold of 5.8-MeV. Ideally for the gamma generator, we would like to select nuclear reactions that produce gamma-rays having energy at or near the peak of the photofission cross section. However, as the gamma-ray energy is increased above 7.5-MeV (the average nuclear binding energy), there can be also be an associated increase in the (prompt) background signal due to the production of photoneutrons from surrounding materials or from Compton scattered source photons. Experiments were performed on a remotely operated 700-keV Van de Graaff ion accelerator system. Figure 3 shows a photograph of the accelerator which is physically located inside a radiation cell having 1-2 foot thick concrete walls and ceiling for shielding. The low-energy (200 keV) accelerator in the front of the photograph is also part of the ion beam system, but is not used in the present experiments. In addition to protons, other ions such as deuterium, ^{3}He, and ^{4}He are also routinely accelerated in this facility. For the present experiments, a 1-10 micro-Ampere beam of up to 700-keV protons bombards a target attached to a water-cooled stage producing mono-energetic gamma-rays from low-energy nuclear reactions (see schematic in Figure 3 for experimental arrangement). Two NaI detectors are used both to monitor the intensity of gamma-rays produced by the target and to detect the prompt or delayed gammas induced by photofission; a ^{3}He detector array is used to count prompt or delayed neutron signals produced by photofission events. Other materials can be placed between the gamma source and nuclear material to simulate intervening cargo or various types of shielding, as well as to measure the background caused by photoneutrons or scattered gamma-rays.

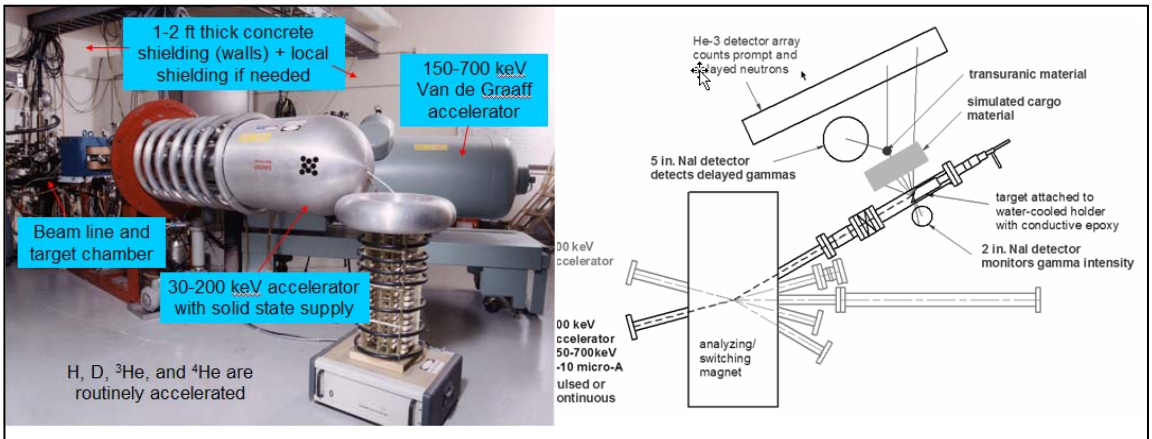

FIGURE 3. Photo on left shows the remotely operated ion accelerator laboratory. Schematic on right shows accelerator experimental setup for measuring gamma yields, background levels, and photofission signals.

4.1. Gamma Yields

Various target materials were tested to determine the corresponding gamma yields and energy spectra over a range of proton energies. Figure 4 shows gamma spectra collected from LiF, Teflon, B_4C, and Mg bombarded with a continuous beam of protons. Each spectrum was collected with a 5-inch NaI detector and normalized to 1-μC of charge.

The (p,γ) target to detector distance was set at 7 cm. Both boron carbide and magnesium have rather low gamma-ray yield which is consistent with the reported ^{11}B cross section value given in Table 1. Magnesium was tested because we could not find a value for its cross section in the literature, but it was reported that a 6.19-MeV gamma-ray (in addition to 4.86-MeV and 0.82-MeV gammas) is produced corresponding to the 317-keV resonance of the ^{25}Mg(p,γ)^{26}Al reaction.[8] While our spectra clearly show the 6.19-MeV gamma-ray, we also see gammas that arise from the higher energy (~8-MeV) branching channels that can occur for the ^{26}Mg(p,γ)^{27}Al reaction. The LiF and Teflon spectra are dominated by the characteristic 6.13-MeV fluorine gamma-ray which was even observed for 250-keV protons from the accelerator (fluorine has a small resonant cross section of ~0.2 mb at 224-keV proton energy). As indicated in Table 1, the resonant reaction for lithium occurs at 441-keV which accounts for the significant jump in the measured yield between the 350-keV and 450-keV spectra. The ^{7}Li reaction is of interest because it produces 17.64-MeV (63% emission/reaction) and 14.74-MeV (37% emission/reaction) gamma-rays which also coincide well with the peak of the photofission cross section. There also appears to be an unidentified, weak low-energy nuclear reaction in Teflon that produces ~12-MeV gammas and may be due to a trace impurity in the material.

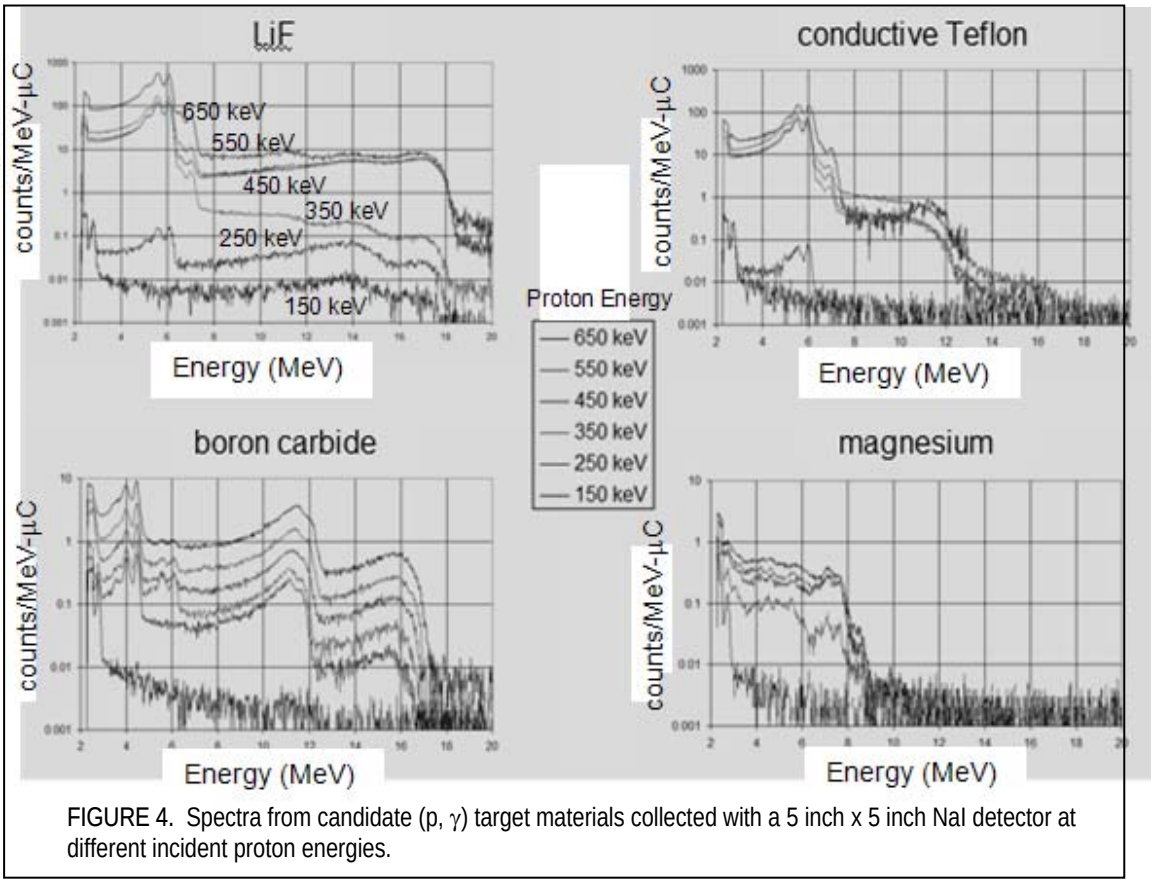

FIGURE 4. Spectra from candidate (p, γ) target materials collected with a 5 inch x 5 inch NaI detector at different incident proton energies.

Accelerator experiments were also performed to determine the gamma-ray yield (fluence) produced by B_4C (boron carbide) and LaB_6 (lanthanum hexaboride). We calculated the relative gamma-ray yield by comparing the stopping powers (eV/atom/cm^2) of each material at the ^{11}B(p,γ) reaction cross section resonance which occurs at 163-keV proton

energy.[7] Taking into account the 80.4% natural abundance of ^{11}B, the calculations indicate that lanthanum hexaboride should have ~55% the yield of pure boron, while boron carbide should have ~77% the yield of pure boron (1.4 times higher than lanthanum hexaboride). For the accelerator experiments, samples of each material were mounted on an aluminum plate and irradiated with a 3-5 μA, 200 keV proton beam. A 5"x5" inch NaI(Tl) detector was placed behind the sample to measure the gamma-ray spectrum (see Fig. 5). Gamma-ray peaks are observed at 4.4, 11.7 and 16.1 MeV having emission probabilities per reaction of 96.5%, 96.5%, and 3.5%, respectively.[8] Although the measured spectrum is somewhat degraded by pair-production (peaks visible near 3.9 and 11.2 MeV) and Compton scattering, it is still possible to integrate these data fairly accurately to obtain the yield of 11.7-MeV gamma-rays. The absolute detector efficiency was calculated as a function of crystal dimensions and source-to-detector distance using a published formula. The absolute gamma yields were 2.3 x 10^8 γ/C for lanthanum hexaboride and 3.9 x 10^8 γ/C for boron carbide. The measured yield for boron carbide was 1.7 times higher than lanthanum hexaboride which is consistent with our computed estimate of 1.4.

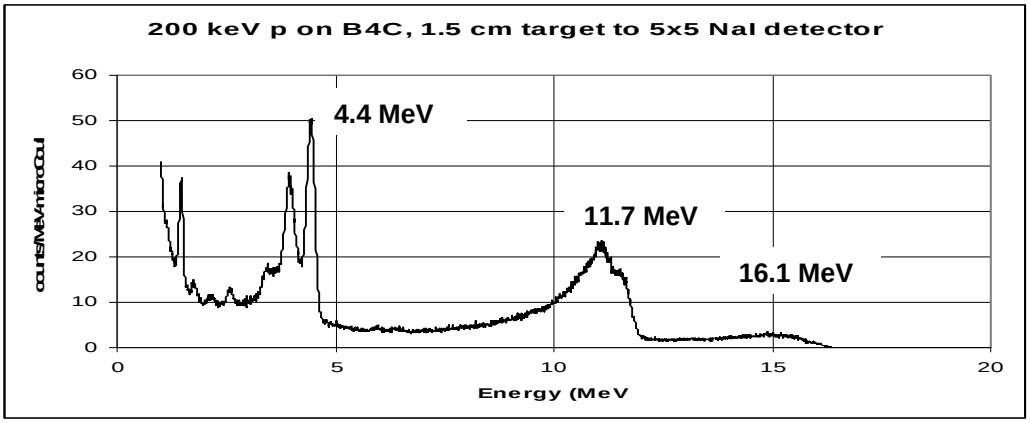

FIGURE 5. Measured gamma-ray spectrum obtained from bombarding a B_4C sample with 200-keV protons.

The spectra from the LiF and B_4C target samples were further analyzed to quantify the total gamma-ray yield as a function of incident proton energy corresponding to each reaction isotope, i.e., ^7Li, ^{19}F, and ^{11}B. The results are plotted in Figure 6 with the assumption that the NaI gamma detector had an absolute efficiency of 15% at all energies. These data indicate that significantly higher proton currents and/or energy are required to achieve high gamma source intensities, especially when using the p-^{11}B reaction. We found that the gamma intensity from the axial gamma tube scales to ~6 x 10^8 γ/s for 1 A (average) current using a LaB_6 target. This latter value agrees well with the accelerator-based measurement of 1.8 x 10^7 γ/C-sr using a B_4C target and is consistent with the expected yield of 10^9 γ/C-sr for a pure ^{11}B target.

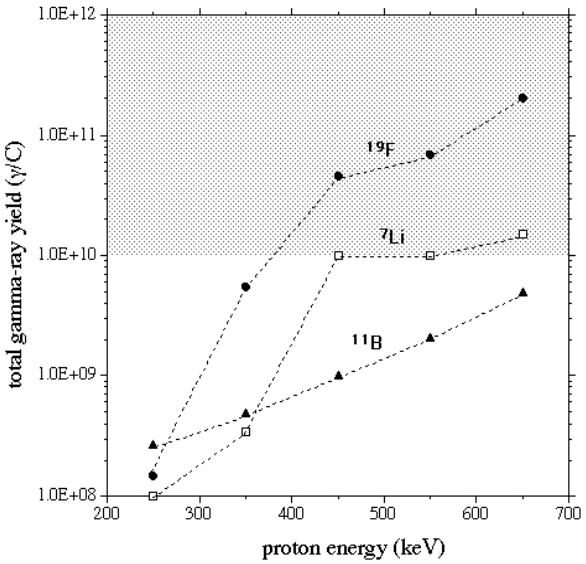

FIGURE 6. The measured total gamma-ray yields from LiF and B_4C as a function of incident proton energy. The dashed lines are to guide the eye.

4.2. Photofission Signatures

Active interrogation relies on stimulating nuclear material to produce radiation signals that can then be detected through intervening shielding material. In gamma-based systems, some fraction of the mono-energetic source gammas will be shifted to lower energies by Compton-scattering and pair production as they pass through intervening material. This can have the effect of reducing some of the "photofission-worthy" gamma fluence at the nuclear material, resulting in a lower detectable signal. The effect can be partially ameliorated by 1) using nuclear reactions that produce high-energy gammas so that the down scattered photons will have energies sufficient to induce photofission and 2) any photonuclear events that occur with surrounding materials will produce energetic neutrons that can also induce fission. An effective active interrogation system must be able to maximize and distinguish the prompt and/or delayed fission signals from the neutron and gamma background that arises from other surrounding materials. For example, the prompt neutron signal can be affected by the photoneutron background caused when the source gammas interact with materials near the object being interrogated. Fortunately, the neutron production cross sections of most nuclear materials are much higher than that of common materials so the neutron background in gamma-based interrogation techniques is fairly low.

4.3. Delayed Gamma Photofission Measurements

Accelerator experiments were performed to detect prompt neutrons and delayed gammas from photo-fission. Figure 7 shows a plot of the data from one of the experiments that measured the delayed gamma spectra using a pulsed proton beam from the accelerator. The beam was electrostatically pulsed at 5 kHz with a 50% duty cycle (100 μs "on" and 100 μs "off") by applying a 500 volt square wave to 75-cm long deflection plates spaced 2.5-cm apart. A 450-keV proton beam bombarded a LiF target located inside a 1.5-inch diameter beamline tube producing 6-MeV (p-^{19}F), 15-MeV (p-^{7}Li), and 18-MeV (p-^{7}Li)

gamma-rays. A large fraction of these gammas struck the depleted uranium sample which consisted of seven 50 mm diameter x 3 mm thick discs (780 g ^{238}U) that were stacked outside of the beamline tube 2-cm from the LiF target. A 5" x 5" NaI gamma detector was positioned 13-cm from the LiF target on the opposite side of the ^{238}U. The detector was electronically gated with a 35% duty cycle (20 μs "on" after proton beam was off and 10 μs "off" before proton beam was on) to capture the short-lived delayed gammas and to avoid any interferences from the source gamma-rays. Beneath the target-uranium arrangement was a plastic-moderated ^{3}He neutron detector array to record the prompt neutron signal. Each photofission-induced gamma-ray spectrum was collected for 100 seconds with 6-μA peak (3-μA average) proton current.

Figure 7a shows delayed gamma spectra collected at three proton beam energies (300, 400, and 500 keV) with and without ^{238}U present. Figure 7b shows the results when each spectrum "without ^{238}U" was subtracted from the corresponding spectrum "with ^{238}U" present. Performing this subtraction removes background contributions such as due to Bremsstrahlung or detector effects. The integrated net signal between 300-keV and 400-keV is computed to be 160 counts/sec and corresponds to the count rate from the fluorine reaction gammas at the 340-keV cross section resonance. Likewise, the increase in net signal between 400-keV and 500-keV spectra (98 counts/sec) corresponds to the Li reaction gammas produced at the 441-keV resonance. Cumulative neutron and gamma count rate results from these accelerator-based experiments are given in Table 3 along with the net photofission signal in each case. The photonuclear cross sections for both depleted and highly enriched uranium (^{235}U) are approximately the same at 6-MeV (p-^{19}F), but the ^{235}U cross section is approximately 2.5 times greater than ^{238}U at 15-MeV (p-^{7}Li). Further, ^{238}U has a significant gamma-ray decay background which is almost non-existent for ^{235}U. Both these effects will improve the signal-to-background ratio for detecting ^{235}U signatures.

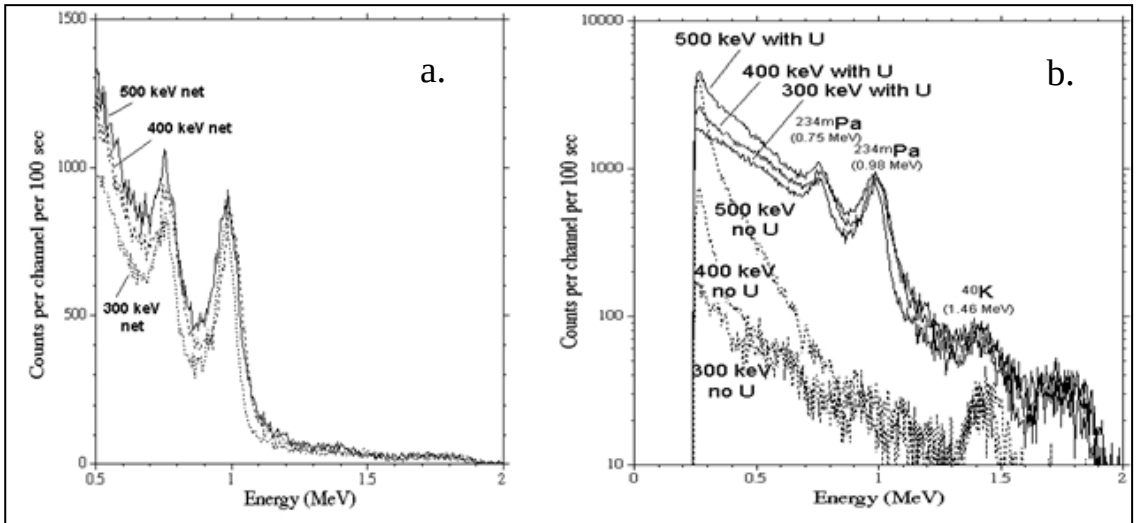

FIGURE 7. Delayed gamma-ray spectra obtained from pulsed photofission experiments of ^{238}U. The spectra plotted in (a) were collected with and without ^{238}U present using a LiF target bom-barded with 300, 400, and 500-keV protons. The data in (b) were obtained by subtracting each spectrum without ^{238}U from the corresponding spectrum with ^{238}U.

To avoid signal interferences, a pulsed photon interrogation source could detect prompt and delayed neutrons (during and between pulses) or delayed gamma-rays (between pulses). Experiments were performed to measure the delayed gamma-ray signal from depleted uranium using the p-^{11}B reaction to produce 11.7-MeV gammas. Delayed gammas were measured using a 1 Hz, 50% duty cycle pulsed proton beam with a 5" x 5" NaI(Tl) detector set to collect a spectrum 10 ms after the beam pulse was off and stop collecting 5 ms before the beam was on. Two depleted uranium disks (234g total mass) were placed immediately behind the target chamber, a distance of 5 mm from the target (see Fig. 8). We exposed the B_4C sample with 4.7 micro-Amperes of protons for 1000s and collected a gamma spectrum. We also collected background spectra under identical conditions (1) with the beam off and uranium present, (2) with the beam on and no uranium, and (3) with no beam and no uranium. After subtracting backgrounds from

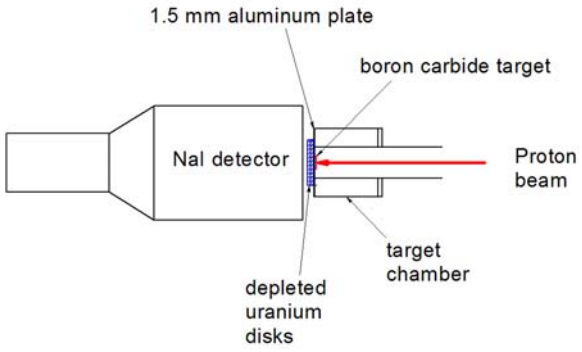

FIGURE 8. Schematic of accelerator experimental arrangement to measure photofission-induced delayed gamma-rays from depleted uranium.

uranium decay, radiation from the accelerator, and the quiescent detector count rate, the net integrated delayed gamma-ray signal under these experimental conditions was determined to be 54 counts in the 3-7 MeV range, 580 counts in the 2-3 MeV energy range and 21142 counts in the 1-2 MeV energy range. While far fewer high-energy delayed gamma-rays were detected, they are attenuated much less by thick shielding (improved interrogation signal detection) and their energies lie above interferences from normal environmental radioactivity (less susceptibility to false positives).

5. MEGAVOLT-ENERGY ACCELERATOR EXPERIMENTS

5.1. Proton Accelerator

Proton beams were produced and accelerated by a 2.5 MeV Van de Graaff ion accelerator. The accelerator is housed in a concrete vault with 1-2.5 foot thick walls for radiation shielding. H, ^{3}He, and ^{4}He are routinely produced and accelerated into a target room with multiple beam lines and end station scattering chambers for different experimental requirements.

5.2. Photofission-Induced Gamma Experiments

Figure 9 shows the end station scattering chamber used for the gamma ray measurements with 3" diameter x 3" long bismuth germinate (BGO) crystal coupled to a photomultiplier tube. Because of residual gamma rays produced by depleted uranium (^{238}U), a 2.8 cm lead shield was inserted between the uranium and BGO detector. The scattering chamber was a six-way cross that contained a CaF_2 target under vacuum. The 6-7 MeV gamma rays from ^{19}F reaction had to penetrate ~1 cm thickness of stainless steel (back flange of the chamber) before striking the ^{238}U. The uranium sample consisted of five sheets of ^{238}U that were each ~0.25 cm thick.

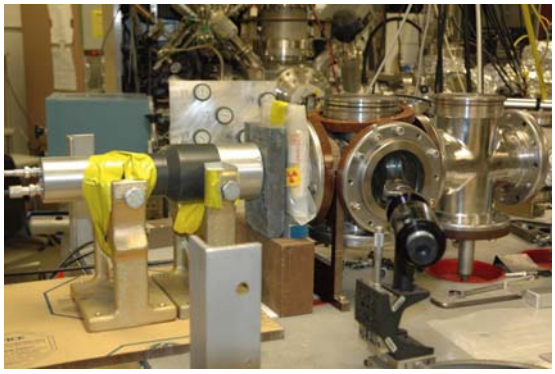

FIGURE 9. Photo of the end station scattering chamber used for the gamma ray measurements. Shown are the six-way cross chamber, the ~1.25 cm of ^{238}U (wrapped in plastic with the radiation symbol on the side), the ~2.8 cm of lead shielding, and the BGO detector. Another accelerator beam line and end station can be seen in the background.

Figure 10a shows the beam spot for 1.8 MeV energy protons on a $LiNbO_3$ target in the high vacuum target chamber. When the CaF_2 target was used in the chamber to generate 6-MeV (p-^{19}F) gammas, it turned black under proton beam bombardment due to the formation of color centers (see Fig. 10b).

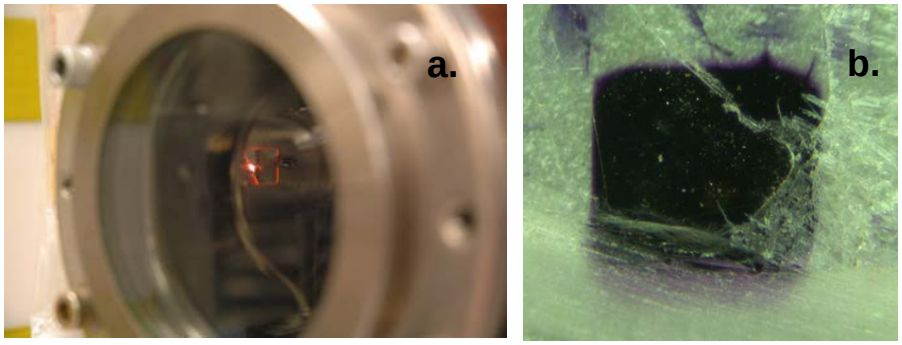

FIGURE 10. a) Beam spot in the target chamber for 1.8 MeV energy protons on a $LiNbO_3$ target. b) Formation of color centers in a CaF_2 target under proton beam bombardment.

Figure 11 shows diagrammatically a first-order method for determining the optimum ^{238}U thickness that produces photofission-induced gammas from an incident gamma source. The optimum thickness corresponds to the interception of the maximum number of source gamma-rays with the least attenuation of the photofission-induced gamma-rays exiting the ^{238}U.

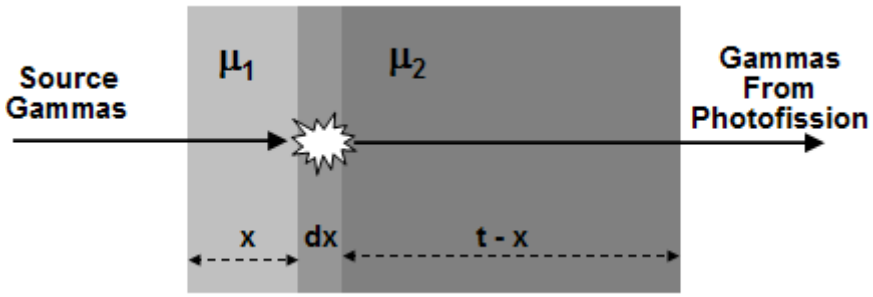

FIGURE 11. Schematic of the geometry used to determine the thickness of ^{238}U that produces the maximum number of detectable photofission gammas.

The yield, *dY*, of gammas in the infinitesimal uranium thickness *dx* is given by

$$dY = N\,\sigma\,\lambda\,C\,\frac{\Omega}{4\pi}\,e^{-\mu_1 x}\,e^{-\mu_2 (t-x)}\,dx$$

where σ is the photofission cross section, N is the number of source gammas, λ is the number of gammas per photofission, C is the concentration of ^{238}U atoms, and Ω is the solid angle to the detector. Integrating this expression over the sample thickness gives,

$$Y = N\,\sigma\,\lambda\,C\,\frac{\Omega}{4\pi}\,\frac{e^{-\mu_1 t} - e^{-\mu_2 t}}{\mu_2 - \mu_1}$$

Setting the derivative of *Y* with respect to *t* to zero and solving gives the optimal thickness, t_{opt}, as

$$t_{opt} = \frac{\ln\left(\mu_2 / \mu_1\right)}{\mu_2 - \mu_1}$$

Since $\mu_1 = \mu_2 = \mu$ = 0.04473 cm^2/g for 6-MeV gammas in ^{238}U, it is straightforward to show that

$$t_{opt} = \frac{1}{\mu} = 1.18\,cm \quad for\ ^{238}U$$

For comparative purposes, the effective thickness, t_{eff}, of ^{238}U corresponding to the thin target approximation is given by $t_{eff} = t_{opt}/e$ = 0.43 cm. In the high-energy accelerator experiments, the sample thickness was ~1.25 cm which is equal to five sheets of ^{238}U.

The BGO detector was calibrated using the 340 keV nuclear reaction resonance of p-^{19}F to produce 6-MeV gamma-rays. The detector's intrinsic efficiency was determined to be

26.8%. The BGO detector was used to measure the gamma-ray output of 2.4 MeV protons bombarding a Ca_2F target at a beam current of ~1 μA. With the inclusion of the 0.71 sr solid angle of the detector with respect to the center of the CaF_2 target, the overall BGO detector efficiency was 1.5%. The number of gammas per μC of charge exiting the end-station scattering chamber was measured to be 2.3E8 γ/μC. In a separate experiment with a biased Faraday cup, the proton beam current was determined to be within 5% of the beam current estimated during the gamma-ray production experiments.

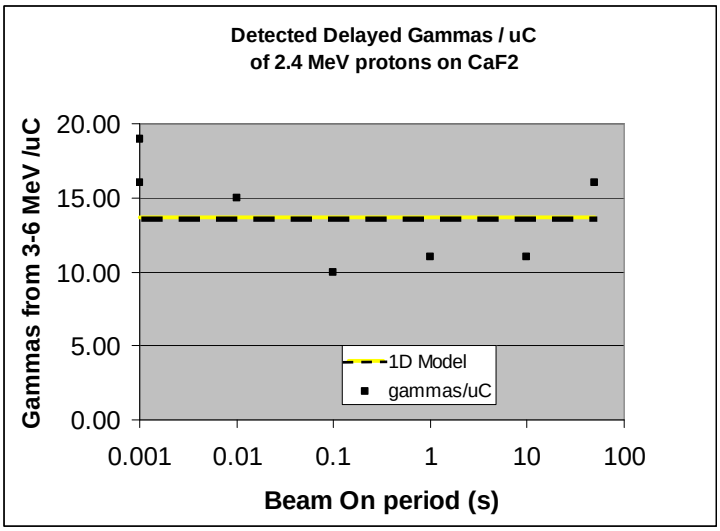

FIGURE 12. Delayed 3-6 MeV gamma rays detected per μC from photofission for 2.4 MeV protons bombarding a CaF_2 target with different proton beam repetition rates.

To reduce the background from prompt gamma-rays, the proton beam was pulsed and delayed gamma rays were measured during off-beam times. The beam on and off times, T, were equal and were changed in the experiments from 100 μs to 100 s in steps of factors of 10. The gamma-ray collection time was 0.8 T leaving 0.1 T before and after the gamma ray collection time. In addition, a lower level threshold of ~3MeV reduced the gamma ray count rate from thorium gamma-rays present in the ^{238}U. The repetition rate of the proton beam was varied from 100 μs to 100 s, but no strong dependence on the repetition rate was found. The delayed photofission gamma ray detection rate of ~14 γ/μC agrees quite well with a one-dimensional theory calculation as shown in Figure 12.

5.3. Photofission-Induced Neutron Experiments

Figure 13 shows the end-station scattering chamber used for the photofission neutron measurements with a ^3He gas proportional counter to detect the prompt neutrons. The scattering chamber was a six-way cross that contained the CaF_2 target under vacuum. The 6-7 MeV gamma rays from ^{19}F reaction penetrated the ~1 cm thickness of the stainless steel back flange of the chamber before striking the ^{238}U. The ^{238}U target consisted of five sheets of ^{238}U that were each ~0.25 cm thick. Neutrons produced from the photofission nuclear reactions were detected by the ^3He gas proportional counter.

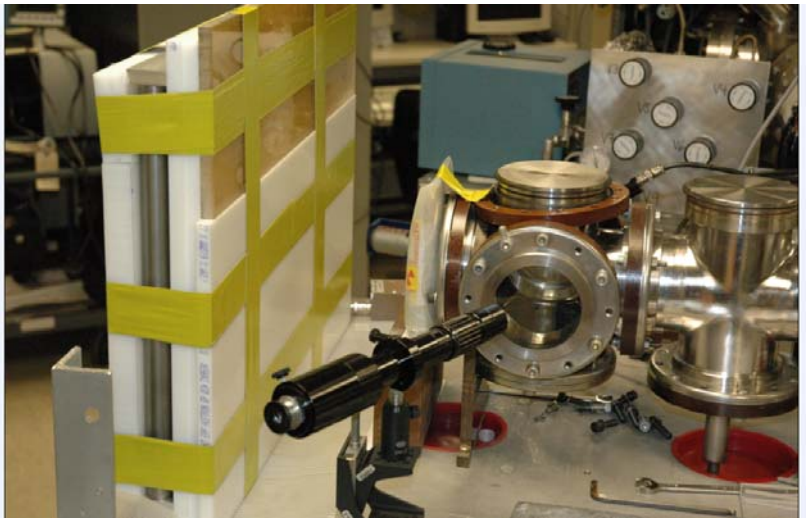

FIGURE 13. Photo of the end-station scattering chamber used to measure prompt neutrons. Shown are the six-way cross chamber, the ~1.25 cm of ^{238}U (wrapped in plastic with the radiation symbol on the side), and the ^{3}He gas proportional counter detector. Another accelerator beamline and end-station can be seen in the background.

The ^{3}He detector was calibrated for efficiency using an AmBe radioactive source with an activity of 5.5E4 n/s. The intrinsic efficiency was determined to be 5.4% and, with the inclusion of the ^{3}He detector solid angle, the overall efficiency was 1.7%. The number of prompt photofission neutrons reaching the ^{3}He detector depends upon the number of high-energy gamma rays striking the ^{238}U target to produce photofission neutrons and the distance from the ^{238}U target to the ^{3}He detector. During the experiments, the prompt photofission neutrons per μC were measured as a function of the position of the ^{238}U target. Figure 14 shows the results of these measurements and a comparison to a one-dimensional model calculation of the expected number of photofission neutrons detected. The simple 1D model over-predicts the measurements by 10-100% indicating that a more rigorous radiation transport physics are needed to account for scattering and other effects.

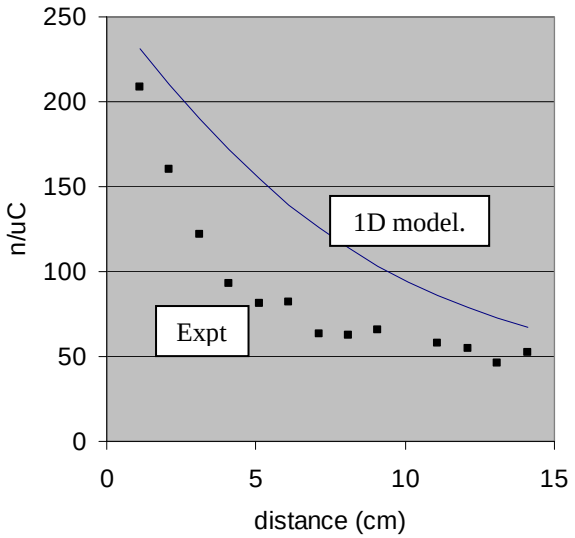

FIGURE 14. Prompt photofission neutrons per μC detected versus the position of the ^{238}U target from the back flange of the target chamber.

In general, the detected rates of prompt photofission neutrons and delayed gamma rays (3-6 MeV) agree fairly well with a one-dimensional model. A 1 μA beam of 2.4 MeV protons on a thick CaF_2 target produced 2.3×10^8 gamma rays per second. Prompt photofission neutrons were produced at a rate of ~100/s for a ~1 cm thick ^{238}U target placed near the $^{19}F(p,\alpha\gamma)^{16}O$ gamma ray source. Approximately 10 delayed gamma-rays per second were produced during the experiments.

6. NEUTRON-PRODUCING NUCLEAR REACTIONS

Existing neutron generators either produce 2.5 MeV neutrons from ^{2}H(d, n)^{3}He reaction (having somewhat reduced penetrating power for hydrogeneous shielding) or produce 14 MeV neutrons from ^{3}H(d, n)^{4}He reaction (creating a strong background from activation of surrounding materials). On the other hand, neutrons with energies between 5 MeV and 10 MeV would be useful in inspection techniques since they are above the threshold for the (n, $n\gamma$) reactions on carbon and nitrogen[9] so, consequently, could be utilized for detecting SNM as well as explosives. A low-energy nuclear reaction that meets the above requirements is ^{10}B(d, n)^{11}C which produces 6.3 MeV. Previous measurements indicated that this nuclear reaction had a very large (>10 mb) total neutron cross section at low (~50 keV) energies.[10] However, there are no corroborating data in the energy region below 200 keV. The next sets of available data start near 400 keV.[11,12] There are more data at higher energies[10,13-15] which show a general trend but have rather large discrepancies between themselves. Sandia teamed with Duke University to extend the cross section measurements of this reaction into the 100-200 kV range which is the typical operational energy of the neutron source.

The ^{10}B(d, n)^{11}C reaction has a Q value of 6.4650 MeV and ^{11}C has five states which can be populated at the incoming deuterium beam energies.[16,17] For a 160 keV incoming deuteron, the maximum neutron energy of 6.3 MeV occurs when the ^{11}C is left in its ground state. Although the five lower energy neutron groups were in principle populated in our experiments, this was not observed. This is because during the experimental run, deuterium accumulated in the target and so resulting ^{2}H(d, n)^{3}He reactions produce significant background neutrons. Ground state neutrons from the ^{2}H(d, n) reaction have an energy near 3 MeV and, thus, the lower energy neutrons from the ^{10}B(d, n)^{11}C reaction were lost in the much larger ^{2}H(d, n) peak. As a result, we were only able to extract a cross section for the n_o channel (6.3 MeV) neutrons.

6.1. Experimental Arrangement

The atomic beam polarized-ion source at Triangle Universities Nuclear Laboratory (TUNL) was used in the present cross section experiments. This source can produce an unpolarized deuteron beam at 80 keV with about 20 μA on target. An accelerator tube and a high-voltage power supply were used to increase the beam energy an additional 60 and 80 keV for total beam energy of 140 and 160 keV, respectively. Due to the accelerator tube bias, the beam current was read out using an optical fiber system which isolated the target from ground. The ^{10}B-target was manufactured by Arizona Carbon Foils[18] by evaporating ^{10}B with a thickness of 1.5 μm on a tantalum backing. Tantalum was chosen partly because it has a similar coefficient of thermal expansion to that of ^{10}B, thus allowing the thin ^{10}B layer to remain intact despite any beam related heating.[19]

The emitted neutrons were detected using six liquid scintillator neutron detectors located approximately 45 cm from the target and placed at 0^{o}, 23^{o}, 45^{o}, 68^{o}, 113^{o}, and 150^{o} with respect to the beam direction. The detectors were 12.7 cm in diameter and filled with BC-501A liquid scintillator. The threshold for each detector was set at the ^{137}Cs edge. The detector efficiencies for the ^{137}Cs edge threshold setting have been modeled very

accurately[20] and have been measured previously at TUNL.[21,22] Pulse shape discrimination (PSD) was used to separate the neutron events from the larger number of gamma-ray events. In the past, this was performed with a long gate/short gate technique. For this experiment, a constant fraction discriminator was used for the rising edge start and a zero-crossing discriminator for tail length. The PSD modules provided very clean separation of the neutrons and gamma-rays from a ^{241}Am-Be source and during the experimental runs. The response functions for the neutron detectors were measured previously at TUNL but at higher neutron energies.[23] Monte Carlo codes were used to generate the response functions at the neutron energies (~6 MeV) where the measurements were made. The simulated response functions agreed very well with the shape of the neutron distributions measured at higher energies as well as those seen during the experiment.

6.2. Data Analysis

After the PSD of the gamma signal, the neutron spectrum for each detector was fit using response functions for the n_o neutrons only. The fitted response function was used to calculate the number of neutrons that passed through each detector during the experimental run. Each of the detector yields was corrected for solid angle, detector efficiency, and dead time, transformed to the center of mass frame and divided by the integrated charge during the run to give a normalized neutron yield. The normalized neutron yields (which are proportional to the differential cross section) were fit with Legendre polynomials up to order $n = 2$. This fit allows a simple integration over all angles which gives the total neutron yield at a given beam energy. The angle integrated neutron yields were fit with the *S* factor formulation to give a total cross section as explained below.

The deuteron beam is very low energy and is stopped completely in the ^{10}B target. Since the cross section is a strong function of energy, it is constantly changing as the deuteron loses energy in the target. The observed neutron yield is the total number of neutrons integrated from the full beam energy down to zero.

Due to both the accumulation of carbon and the increase with time of the ^{2}H(*d*, *n*) background, a new target was placed in the beam periodically and only the first several hours of beam exposure were used for analysis. During that time, the effect of both processes was small. In addition, the energy of the incident deuterons was changed every hour to either 140 keV or 160 keV in order to monitor changes in the neutron yield over time for both energies and also to provide neutron yield ratios where the amount of carbon buildup would not differ significantly from run to run.

6.3. Experimental Results

The data were analyzed by assuming a constant astrophysical *S* factor below 160 keV. This procedure makes it possible to extrapolate the cross section to lower energies which is important for the calculation of the neutron yield from a thick target. The *S* factor analysis gave $S = 11420 \pm 230_{stat} \pm 2600_{sys}$ keV b. The statistical error in the *S* factor is about 2%. The systematic error of about 23% is dominated by the detector response function fitting error but also includes effects from solid angle, charge integration,

detector efficiency and carbon accumulation. The carbon accumulation rate was adjusted and is consistent with the deuteron elastic scattering energy loss and cross section measurements. As the deuterons travel toward the ^{10}B target, they lose energy passing through the carbon buildup. Since the calculated amount of carbon buildup was different for each of the six one hour long runs, the deuteron energy at the surface of the ^{10}B was different for each run. With time, the deuteron energy was degraded more and more leading to different "effective" energies. The cross section was calculated as a function of the deuteron laboratory energy (degraded by the carbon buildup) using the fitted constant *S* factor. At low energies, the results are totally inconsistent with the previous Brookhaven measurements.[10] However, the previous experiment reports a total neutron cross section and the present result is for n_o neutrons only. The distorted wave Born approximation (DWBA) and Hauser-Feshbach calculations were both used to calculate the n_o part of the total neutron cross section. The DWBA calculation predicts the n_o fraction to be approximately 20% while the Hauser-Feshbach calculation predicts approximately 30%. Both calculations predict the n_o part of the total neutron cross section to be non-negligible and certainly not the several orders of magnitude smaller it would have to be in order to be consistent with the previous data. Furthermore, since the deuteron beam stops in the target, a large cross section at lower energies as reported in Ref. 10 would reveal itself through the observation of a larger-than-expected number of neutrons as well as a constant neutron rate at deuteron energies of 160 and 140 keV. The large drop-off in count rate between 160 and 140 keV places a limit on the size of the cross section at lower energies. The cross section for the n_o channel at and below E_d = 50 keV must be less than 30 mb in order to be consistent with the 160 and 140 keV data within the total errors. Even at the few percent level of contribution to the total neutron cross section, this implies a value for the total neutron cross section which is less than a few micro-barns at low energies. The disagreement with the previous data can perhaps be explained since the cross section results at low energies were at the limit of sensitivity of the experiment. It was an activation experiment and the authors reported seeing no production of ^{11}C at the low energies.[10]

The present measurement of the ^{10}B(d, n_o)^{11}C cross section gives a value of ~2.0 ± 0.5 μb at E_d = 160 keV. This value is at least 3 orders of magnitude smaller than the lower energy total neutron cross section data from Ref. 10. Unfortunately, the low cross sections means this reaction is not practical for a neutron interrogation source, at least not with deuteron beam currents on the order of tens of microamps. However, the results are consistent with the predictions of a Hauser-Feshbach treatment of the reaction suggesting a statistical compound nucleus reaction rather than a direct reaction.

7. INTERROGATION SOURCE DESIGN

As mentioned earlier, the FIND interrogation source is based on using low-energy nuclear reactions to produce high-energy particles, i.e., a process called "nature's nuclear amplification". Although isotopic sources release neutrons by radioactive decay, their intensities are generally too low to be suitable for an active interrogation system. At the other extreme, the most intense neutron sources are fission reactors or high-energy particle accelerators (the latter spallation-type sources use proton beams to break up heavy nuclei in a target). These large, complex, and costly installations yield copious amounts of neutrons at energies up to hundreds of millions of electron volts, but would be impractical to operate and maintain as part of an active interrogation system. High intensities of neutrons can also be produced by a neutron tube (generator) which is essentially a miniature, low-energy accelerator that produces neutrons by hitting a metal or hydrided target with deuterium or tritium ions. A fusion reaction occurs between the deuterium in the beam and deuterium or tritium in the target (D-D or D-T reactions) resulting in a high flux of energetic neutrons. One of the drawbacks in typical commercial neutron tubes is the short operational lifetime due to the target becoming depleted of the hydrogen isotopes.

Many of the limitations in conventional neutron generators have been overcome in a design that uses a miniaturized plasma ion source, driven by a radio-frequency (rf) antenna, to efficiently produce a high current of deuterium ions.[24] More than 90 percent of the deuterium ions in the plasma are monoatomic with energies at the peak of the reaction cross section compared to other ion sources which typically only have about 20 percent mono-atomic ions. The target in these rf-driven neutron tubes consists of a thin sheet of titanium bonded to a copper substrate with water-cooling channels. New deuterium ions are being continually added ss the beam hits the target, so the target does not become depleted and the tube has long operational lifetime. The highest yield system has achieved intensities of ~10^{11} n/s.[24]

7.1. Axial Gamma Source

The (p,γ) reactions in Table 1 require a gamma generator to operate at higher proton voltages than compared to existing neutron tubes. To achieve higher energies, we implemented a prototype gamma tube design based on a simple axial accelerator column concept. The gamma generator was designed, built, and tested in a project funded by the DOE Office of Nonproliferation Research and Development (DOE/NA-22). The gamma tube (see schematic and photo in Figure 15) utilizes an rf induction ion source, a multi-electrode acceleration column, and boron-containing target. The $^{11}B(p,\gamma)^{12}C$ nuclear reaction has a well-known resonance at 163 keV proton energy, having a cross section of 156 μb and width of 7 keV. The reaction produces a pair of 4.4-MeV and 11.7-MeV gammas 97% of the time and 16.1-MeV gammas 3% of the time. Both the 11.7-MeV and 16.1-MeV gammas are above the threshold for photofission which is approximately 6-MeV. The 163 kV voltage needed for the reaction necessitated the use in the gamma tube of an acceleration column, differential pumping system, and pressurized vessel that could enclose the high voltage column. Several boron-containing materials were initially considered for the gamma tube target including sintered boron carbide (B_4C),

natural boron, and lanthanum hexaboride (LaB_6). LaB_6 was selected due to its high thermal conductivity and low resistivity. The target consisted of a 3 mm thick, 5 cm diameter sintered LaB_6 ceramic disk mounted on a copper water-cooled plate with a thin layer of liquid indium-gallium acting as a thermal interface for better heat conductivity.

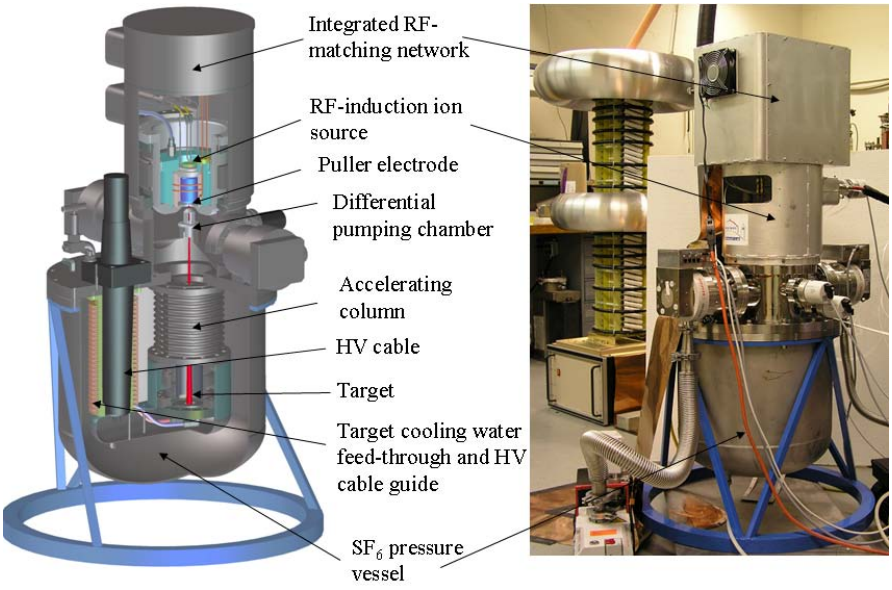

FIGURE 15. On the left is a cut-away schematic of the axial-type gamma tube. On the right, the gamma tube is shown in the laboratory with the high voltage power supply behind it. The dimensions of the gamma tube are 40 cm in diameter and 100 cm in height.

7.1.1. Spectrum Measurement

Figure 16 shows gamma spectrum measured from the gamma tube using a 3" x 3" NaI detector. For gammas at these high energies, pair production begins to dominate and the difficulty in fully absorbing the pair products and annihilation photons can be seen in the spectrum. Energy detection losses from the production pair's bremsstrahlung emission and lower detection efficiency at higher photon energies contribute to the broadening of higher energy peaks.

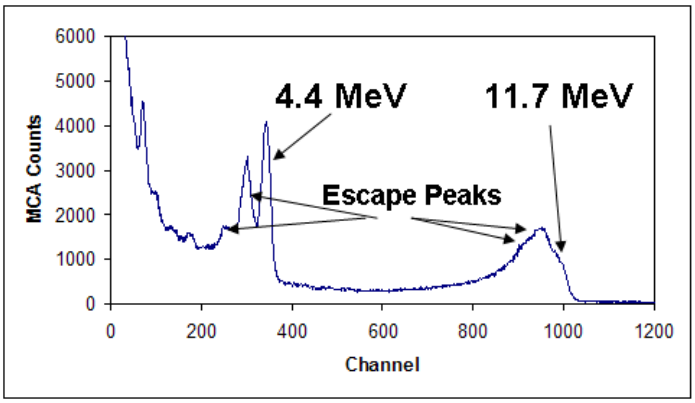

FIGURE 16. Measured gamma spectrum from the axial gamma tube using a 3" x 3" NaI detector. The 4.4 MeV p-^{11}B peak produces two lower-energy escape peaks due to pair production. The 11.7 MeV full energy peak is the slight bump near channel 1000 and the 16.1 MeV peak cannot be resolved with this detector. The spectrum was collected for 30 minutes at a beam current of 0.74 mA and acceleration voltage of 169 kV.

7.1.2. Yield Measurement

The process to extract the gamma yield from the measured spectra involved integration and normalization utilizing associated MCNPX model results. The MCNPX model was initially validated to the measured gamma ray spectrum. Figure 17 shows the model for the gamma tube used in the simulations. Most of the materials which have high gamma attenuation coefficients (e.g., metals) in the gamma tube were included in the model while less attenuating materials/structures (e.g., ceramic insulators) were ignored. For the MCNPX source definition, a Gaussian energy broadening coefficient was defined due to normal energy resolution losses from the NaI detector. These losses can come from non-uniform light collection to photomultiplier noise.

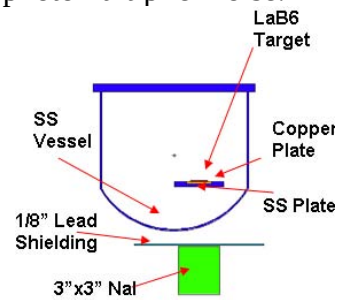

FIGURE 17. The gamma tube model used in the MCNPX simulations.

The coefficient was estimated by a best-fit method from experimental spectra. The deposited energy from all gamma-ray interactions in the detector were tallied and binned. Figure 18 shows the MCNPX computed spectrum compared to experimental result. The simulated spectrum deviates from the experimental result in the range 0 - 3.5 MeV and also in the range 4.4 - 9.5 MeV. The elevated low-energy gamma counts are due to scattering of gamma rays from all materials from the room and gamma tube. The MCNPX simulation does not model all the materials so a discrepancy occurs at low energies. In the intermediate energies between 4.4 and 9.5 MeV, the discrepancy may originate from the $^{19}F(p,\alpha\gamma)^{16}O$ reaction. The gamma tube pressure vessel contains 80 psig of sulfer hexafluoride and the fluorine reaction produces a 6.13, 6.92 and 7.12 MeV gamma ray. To determine the gamma yield, the experimental spectrum was integrated between 10 and 12 MeV and compared to the integrated MCNPX value. Because the MCNPX generated output has units of per source gamma, the output could be normalized to the experimental value and time.

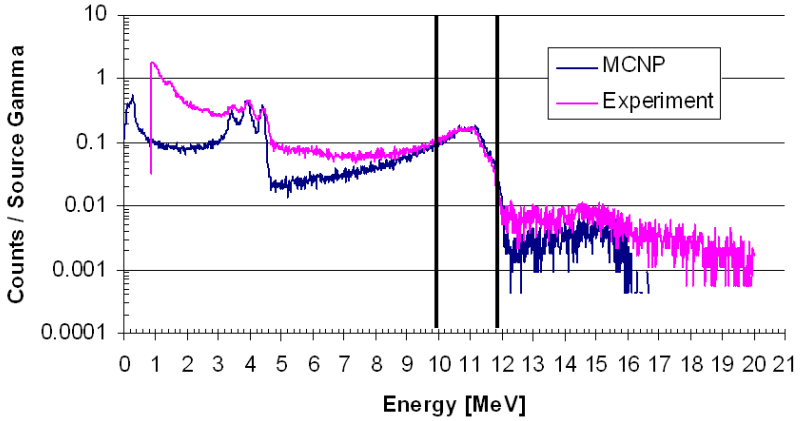

FIGURE 18. Graph showing the experimental and MCNPX spectra. An energy window, depicted as lines at 10- and 12-MeV, was used to determine the gamma yield.

The gamma yield as a function of proton current was measured with a 3" x 3" NaI(Tl) detector; angular distribution measurements were made at different orientations using a combination of 3" x 3" and 2" x 2" NaI(Tl) detectors. In the former case, the detector placed on-axis and 3" below the bottom of the gamma generator pressure vessel corresponding to having the detector 9.25" from the top surface of the target. With 1 mA of beam current, the gamma yield into 4π was measured as 2.0E5 γ/s. The yield, as seen in Fig. 19, has a slight upward curve at higher beam currents. This is due to an increase in monatomic hydrogen produced by the ion source at higher rf powers. Assuming a best fit line for the yield versus current, the gamma intensity would scale to ~6.0E8 γ/s for 1 A (average) current. This latter value agrees well with our previous accelerator-based measurement of 1.8E7 γ/C-sr using a B_4C target (see Section 4.1).

7.1.3. Yield Angular Dependence

The angular dependence of the gammas generated in the gamma tube was measured using a 3"x3" in NaI detector placed at 0 and 60 degrees relative to the proton beam axis, while a 2"x2" NaI detector was kept in a stationary position at 90 degree orientation. The integrated output from the 2" x 2" detector was used to normalize the data collected with the 3" x 3" detector due to the repositioning at different angles. Only the 11.7 MeV gamma-ray was analyzed for the results shown in Fig 19. The average intensity ratio between 60 and 0 degrees (I_{60}/I_0) was 91 ± 0.7%. An expression for the normalized yield as a function of angle was given as $Y(\theta) \sim 1 + 0.23 \cos^2\theta$ so the expected gamma intensity ratio was 86%.[25] The gamma yield was also measured using an ion accelerator as a function of angle. The target consisted of a disk of 3 mm thick LaB_6 affixed to a 1.5 mm thick aluminum plate. A 3"x3" NaI detector was placed 9" behind the aluminum plate inline with the incident proton beam and a 2"x2" NaI detector was positioned 2" behind the plate at 135° relative to the front surface of the target. Hydrogen ions were accelerated to 400 keV and the total beam current on target was 1.3 μA. In this case, the measured angular intensity ratio was found to be 86 ± 0.3% , which agrees with the measurement from the gamma tube.

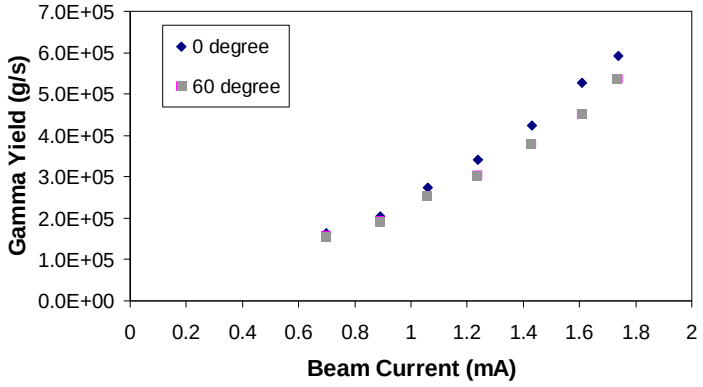

FIGURE 19. Plot of the measured gamma intensity versus proton current with the detector orientated at two positions relative to the axis of the gamma tube. The bias voltage was 175 kV. Statistical counting errors are smaller than the data point values.

7.1.4. Photofission Measurements

Depleted uranium (DU) was placed directly beneath the gamma tube vessel and approximately 20 cm from the LaB_6 target. A 3/16" thick lead sheet separated the uranium from the ^3He detector. The main purpose of the lead was to minimize electromagnetic fields that were created from occasional high voltage sparking from coupling into the detector electronics. There were fourteen 116 g disks of depleted uranium that were evenly spread out on top of the lead sheet. The neutron detector was comprised of fifteen 1" diameter ^3He tubes placed in a polyethylene moderator with built in preamplifiers. The detected photofission neutron signal was determined subtracting cosmic-induced photoneutrons from DU and lead, decay neutrons from DU, natural room background and photon induced neutrons from the generator while in operation. The natural background count rate was measured to be 2 c/s, and the background count rate with DU and lead in place was 4 c/s. Table 3 shows the measured neutron count rate compared to MCNPX simulation results. In the experiments, the photofission-induced neutron signal could not be distinguished from photon induced neutrons from DU and lead. However, the modeling results show that the photon induced neutrons in lead more than doubled the neutrons produced from the depleted uranium disks.

TABLE 3. Neutron count rate as a function of the beam current.

Beam Current (mA)	Measured Neutron Count Rate (n/s)	MCNP Neutron Count Rate (n/s)
0.72	2.6	2.8
1.07	3.7	5.9
1.42	7.8	9.0
1.72	11.3	11.7

7.2. Coaxial Gamma Source

A high power coaxial gamma generator was designed and built in a project funded by the Department of Homeland Security / Domestic Nuclear Detection Office / Transformational and Applied Research Directorate (DHS / DNDO / TARD). Similar to the axial gamma source above, lanthanum hexaboride (LaB_6) was used for the target because it is a rigid ceramic material with good thermal shock resistance and adequate electrical conductivity. The challenge for the high power gamma source design utilizing the $^{11}B(p,\gamma)^{12}C$ reaction is the need to operate with high proton current because of the small gamma production cross section (0.16 mb) at the 163 kV resonance. The design goals for the prototype generator included a time-averaged beam current of ~1 A at an acceleration voltage of 180 kV and the capability of pulsed operation at 500 Hz and 20 μs pulse length for a duty factor of 1%. The design

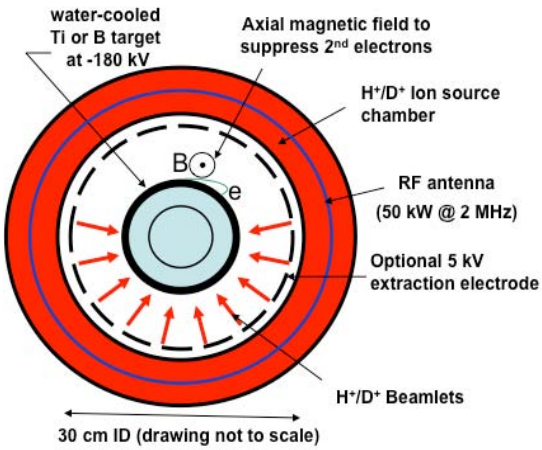

FIGURE 20. Schematic showing the coaxial gamma/neutron source concept.

goals for neutron source operation include the same pulsing scheme with a 1% duty factor, but at a significant lower time-averaged current of 100 mA for the generation of 10^{11} n/s via the D(d,n)^{3}He reaction.

RF-driven ion sources have been shown to be capable of producing high extracted beam current with atomic ion species exceeding 90%. The high peak current needed for pulsed operation requires a large extraction area and a large volume ion source. For this reason, the coaxial design was adopted with a toroidal-shaped plasma chamber (inner diameter of 30 cm) surrounding a cylindrical gamma production target shown schematically in Figure 20. RF-power is coupled into the plasma through an internal antenna. The beam is extracted from the source (at ground potential) through a slotted grid with a large, total extraction area. The target is at high potential, which generates an electric field that extracts the ions from the plasma chamber and accelerates them across a single gap onto the target. An optional extraction electrode can be installed for gating the beamlets to achieve fast rise and fall times. The gamma production target consists of LaB_6 sheets that are attached to a water-cooled backing. Magnetic field suppression is employed to prevent the back streaming of secondary target electrons. The target voltage is provided by a capacitor bank that is charged by a dc power supply.

The coaxial gamma generator consists of a toroidal-shaped plasma chamber (see three-dimensional computer design shown in Figure 21a) surrounding a cylindrical gamma production target. The plasma discharge is driven by a 2 MHz rf-power supply capable of delivering up to 50 kW and uses an internal rf-antenna consisting of a conductor inside a water-cooled quartz tube. The antenna shape resembles a stretched winding that is bent around the toroidal chamber as seen in Figure 2b. Permanent magnets embedded in all three walls of the plasma chamber generate a multi-cusp field that confines the plasma and allows higher plasma densities while operating at lower gas pressures.

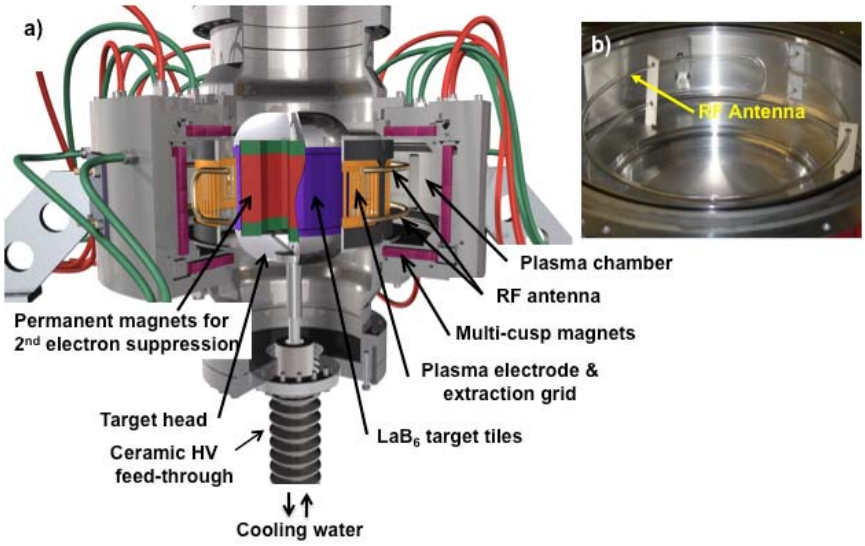

FIGURE 21. Gamma generator with toroidal-shaped plasma chamber and low-power gamma production target: a) schematic drawing, b) quartz RF antenna inside plasma chamber /neutron source concept.

The plasma chamber is at ground potential and a negative 180 kV voltage is applied to the cylindrical target at the center of the generator for accelerating the ions toward the target. A 180 kV, 267 nF capacitor bank, built for pulsed operation, can supply a 100 A peak current for 20 μs with a 4.2% HV droop. Proton beamlets are extracted through 92 slits in the concentric plasma electrode that are 60 mm long and 5 mm wide resulting in a grid transparency of ~50%. The pressure in the acceleration gap needs to be in the low mTorr range to ensure HV holding. This is achieved by operating the ion source at low gas pressure (< 5 mTorr) and by pumping the acceleration gap with a turbo pump that is mounted on top of the generator chamber. A filament is provided for assisting plasma ignition and pulsed operation at low gas pressure.

Ion optics simulations were performed to calculate the ion trajectories of the extracted beamlets. The results, as shown in Figure 22, were used to determine the dimensions of the aperture slit, the acceleration gap distance, and the spot size on the target surface. The trajectories of secondary electrons emitted from the target surface in a suppressing magnetic field were also computed to optimize the field strength and the arrangement of the permanent magnets around the chamber.

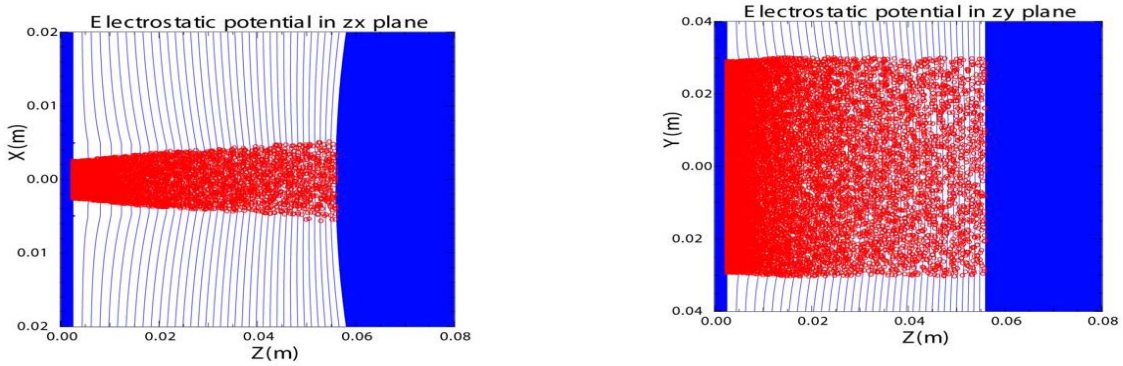

FIGURE 22. Computer simulation of the extraction and acceleration of a sheet beam (1 slit) from the ion source to the target. The left diagram shows the beam profile in the narrow slit direction. The beam profile in the wide direction is shown on the right.

As mentioned above the target consists of LaB_6 tiles that are brazed to a water-cooled cylindrical structure. In particular, it was found that LaB_6 could successfully be brazed onto a copper substrate. The target cylinder with a diameter of 20 cm is mounted on a stem in the center of the toroidal plasma chamber. The cooling water is brought into the target through a ceramic, vacuum-tight high voltage (HV) feedthrough. A low-power target was built for test operation at 1 Hz. Finite element heat transfer calculations have been performed for the design of a high-power target consisting of LaB_6 tiles brazed onto a thick copper backing. The calculation showed that the heat load from the full-power, pulsed ion beam (100 A peak current, 1% duty factor) resulted in average and instantaneous temperatures of the LaB_6 that were within acceptable limits.

The prototype coaxial gamma source was designed and built for low duty factor experiments such that testing can be done with a low current 200 kV power supply at 1 Hz repetition rate. Figure 23 shows the device mounted in a test stand. The ion source

was designed to deliver the desired high peak current for testing the basic operational functionality.

FIGURE 23. Coaxial gamma generator installed in the test stand. The lower, larger diameter chamber is the plasma chamber with the target mounted at its center. The turbo pump is seen mounted directly on top of it. The HV connection is from below.

In initial tests, the ion source could be ignited and operated in pulsed mode with 45 kW RF power at 8 mTorr hydrogen gas pressure. Further testing and optimization of low-pressure operation is needed. During high voltage conditioning of the apparatus 170 kV across the acceleration gap were reached with the ion source pressure at 8 mT, and with the target at positive polarity. High voltage holding was compromised when the target was at negative polarity, presumably due to the target's electron-suppressing toroidal magnetic field. It is planned to change the magnetic configuration into a multicusp field to eliminate the discharge problem. Higher gamma yields will likely require a device operating at accordingly higher beam currents and power levels.

8. MODELING AND SIMULATION

An optimal design for a field-deployed FIND system requires an assessment of the most useful radiation signatures, the best detectors and data collection methods, and the signal processing. In parallel with the above experimental results, we initially evaluated the performance of a neutron/gamma source for detecting shielded SNM using a "zeroth-order" analytical model that captures the essential nuclear and transport effects, but does not include the detailed, and more computationally intensive, models found in advanced radiation transport codes. Since other studies have examined the performance of neutron- and bremsstrahlung-based sources for active interrogation of lightly or unshielded nuclear material,[26-30] our focus has been on determining the fission-induced signatures in different shielding scenarios using the D-D neutron and mono-energetic gamma-rays from our source. The simulations were performed with the following interrogation particles and energies: 6.1 MeV gammas from the $^{19}F(p,\alpha\gamma)$ reaction, 11.7 MeV gammas from the $^{11}B(p,\gamma)$ reaction, 17.6 MeV gammas from the $^{7}Li(p,\gamma)$ reaction, and 2.5 MeV neutrons from the $^{2}H(d,n)$ reaction. In the simulations, the particle intensities were limited by the maximum proton or deuteron current in the source generators which was assumed to be one Ampere. The performance of each source for interrogation also depends on inspection procedure itself. For example, in a mobile application, the detectors will most likely be on the same side of the source with respect to the cargo container but, in this case, the background might be less if the detectors and source were on opposite sides of the container (like in a fixed site system). Additionally, inspections could be done by interrogating a large area of the container or by collimating the source beam and scanning with a small spot. While "spot" scanning improves the signal-to-background ratio, the inspection time will be significantly longer.

We modeled different interrogation scenarios corresponding to different shielding materials (cargo) in the container. In particular, the following shielding configurations were simulated: 1. Empty container, 2. Polyethylene (ρ = 0.93 g/cm^3), and 3. Iron (ρ = 1.68 g/cm^3). For each scenario, we determined the so-called ROC (Receiver Operator Characteristic) curves that give the relationship between detection probability, false positive probability and inspection time. The ROC curves were obtained by computing the Background (B) that reaches the detector when no SNM is present and the Background + Signal (B+S) when SNM is present. Both of these quantities depend on and affect the inspection time needed to achieve a particular detection probably.

Figure 24 shows example statistical distributions for B and B+S which are assumed to be Gaussian in shape. Depending on where the threshold (vertical line in figure) is set, the model will determine the tradeoff between the false positive (FP) and the detected (D) fractions or true positive fractions. Increasing the statistics causes the Gaussians to become narrower, leading to fewer false positives as expected. For a given detection fraction (e.g., we compute results for D = 0.90, 0.95 or 0.99), a different FP is obtained as function of the background or as function of time for a given background rate. From the resulting ROC curves, we obtain an estimate of the inspection time necessary to minimize the FP rate. We note that, for actual container inspections conducted in the field, every

false positive will require a secondary inspection with the commensurate slowing down of overall container throughput.

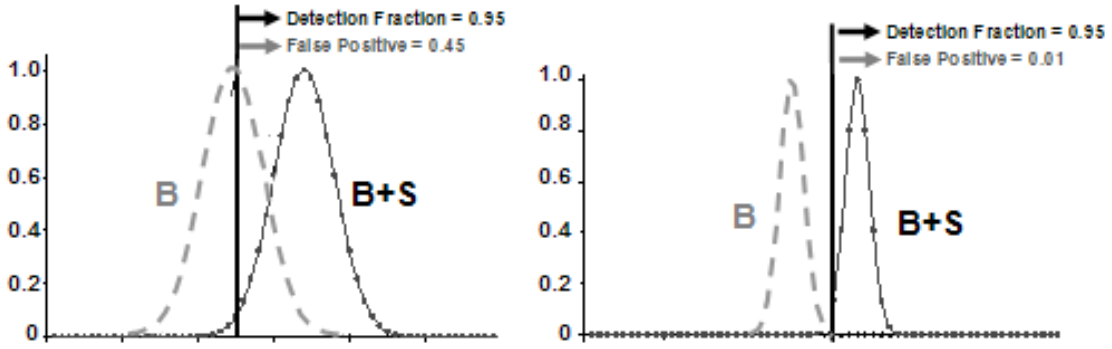

FIGURE 24. Gaussian distribution representation of the false positive fraction statistics.

There are two kinds of time and energy dependent signals coming from the irradiated cargo container: prompt and delayed particles, either gammas or neutrons. The prompt particles can be detected with a continuous irradiation of the cargo (Duty Cycle = DU = 1). The delayed particles inspection procedure requires a probing pulse followed by an "off" interval during which the detectors are sensing the delayed signals coming from the container. The duration of these intervals may vary according to the kind of interrogation required. Many of the delayed fission signals occur within 100 microseconds from the exciting pulse, so a 50% irradiation duty cycle (DU = 0.5 with 100 μs on and 100 μs off) is suitable and this is the pulse mode that was used in the simulations. We can also envision detection methods that require a much longer "off" time between pulses, such as the measurement of the differential die away neutron signal (when using a neutron interrogation source) which can last several milliseconds (e.g., an "on" pulse of 100 μs followed by an "off" period of 10 ms).

As detectors measure both energy and arrival time within their response function limits, the models also take into account both energy and time and, for each, evaluates B and S/B. For example, it is possible to count the detected delayed gammas or neutrons and differentiate between those originating only from SNM and those originating from surrounding materials. The total background B consists of two parts: the "induced" background B_I and the "constant" background B_C ($B = B_C + B_I$). The constant background originates from cosmic rays, environment (terrestrial radiation), and detector-electronics noise. The flux of cosmic muons at sea level is ~100 muons/m^2/s and, since most detectors will respond to this flux, it sets a floor on the background count rate in a detector. Although the muon signal could be removed through an anti-coincidence setup, such an arrangement would be too large and demanding from a practical standpoint to be viable for general interrogation applications. The normal sea level radiation background due to terrestrial soil radioactivity (e.g., thorium decay) consists primarily of ~300 keV gamma-rays having an average flux of 18 γ/cm^2/s, which is significantly larger than the cosmic flux. Some detectors will respond to this signal while others are blind to it. In the

present analysis, we consider only these latter "blind" types of detectors. We also assume that the electronic noise is negligible and the detection efficiency is approximately 10%. With the above contributions to the background, a 1 m^2 detector will have a constant count rate of about B_C = 10 counts/s. In the ROC curve analysis B_C is given by B_C = 10 x DU so that 10 counts/s is used in the case of prompt signal detection and 5 counts/s is used in case of delayed signal detection. The induced background, B_I, originates from surrounding materials and contributes primarily to the total prompt signal in the detector. B_I is proportional to the probing flux as is the actual signal count rate (S) that the detectors are trying to distinguish. It is useful to estimate the minimum detectable signal for a given false positive value (FP) and acceptable inspection time when the background (B) is simply B_C. ROC curves are shown in Figure 25 for the two cases of B_C = 10 counts/s (prompt detection) and B_C = 5 counts/s (delayed detection). In this case, if we assume the required FP is no larger than 0.001 and the allowable interrogation time is up to 90 minutes, then the ROC analysis indicates that the minimum detectable signal rate (95% detection probability) will be 0.2 counts/s (S/B = 0.02) for prompt particles and 0.15 counts/s (S/B = 0.03) for delayed particles.

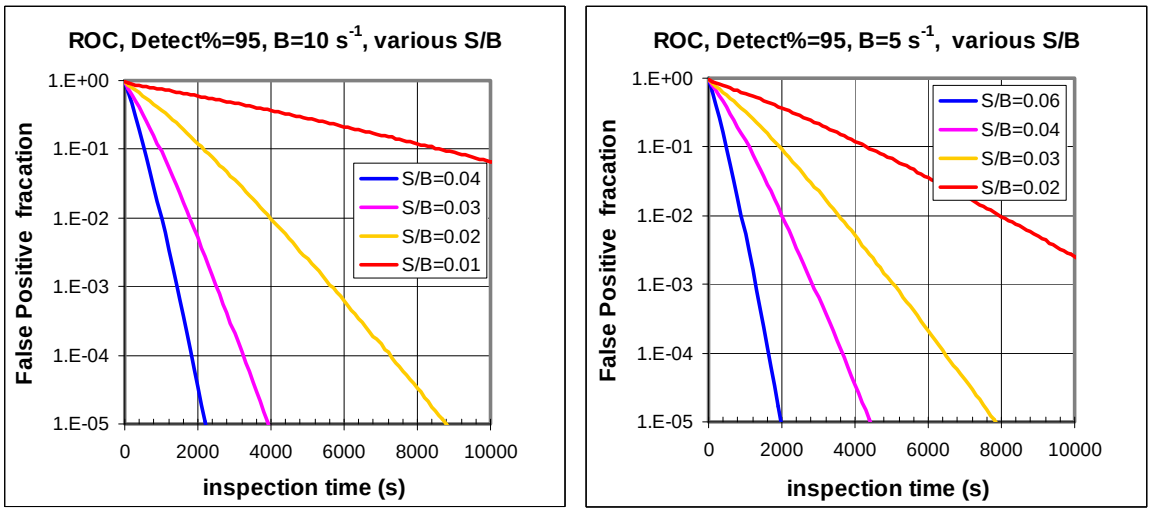

FIGURE 25. ROC curves for various S/B ratios when B = B_C. Plot on left is for B = B_C = 10 (prompt signal detection) and plot on right is for B = B_C = 5 (delayed signal detection).

One contribution to the prompt induced neutron background (B_I) for the gamma source is due to the production of photoneutrons from the container and its contents. As seen in Figure 26, the thresholds for isotopes such as ^{56}Fe, ^{13}C, deuterium, and ^{6}Li extend down to the megavolt-energy range. Other contributions to B_I are the non-absorbed source particles that interact directly with the detector (shielding would be placed between the interrogation source and detector) and source gammas that are multiply-scattered by the cargo. Fortunately, these latter background contributions are relatively small and, therefore, not considered below. It is clear from Fig. 26 that a 6-MeV gamma source (i.e., using the p-^{19}F reaction) will cause the smallest B_I since the photon energy is below most photoneutron thresholds. The background from a source using the p-^{11}B (12 MeV gammas) or p-^{7}Li (15,18 MeV gammas) reactions could be reduced by collimating and scanning with a small (pencil) beam, but this will be at the cost of increasing the overall

inspection time. Delayed signals are not affected by any of the prompt effects above so, in this case, B is constant and simply equal to B_C.

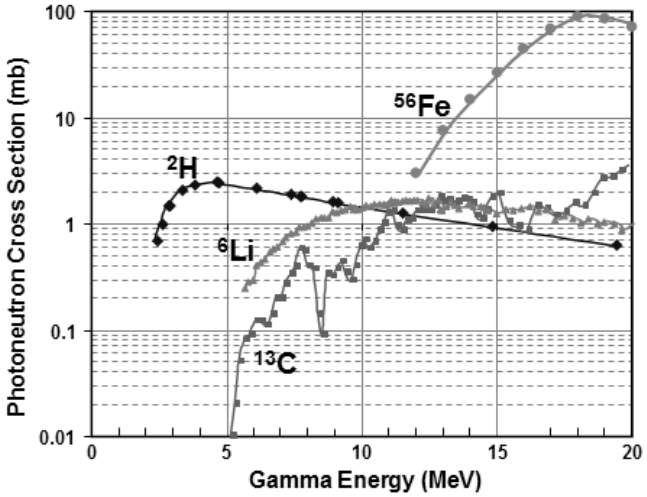

FIGURE 26. Photoneutron cross sections of some isotopes near threshold.

Figure 27 shows a schematic of the cargo container model. The source is located 1 m from the container wall, the detectors are co-located with the source, and the uranium sphere is at the center of the container.

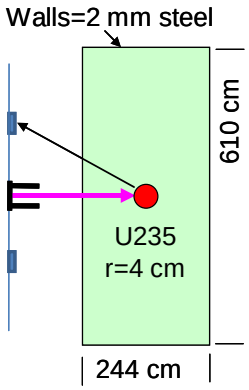

FIGURE 27. Schematic of cargo container model.

The tables below shows the predicted fission rate generated by the sources discussed previously, in each of the design basis threats. While it is best to get the largest number of fissions at the lowest dose, examination of the tables shows that a D-T neutron source produces adequate fission rates for all threats except the poly case. The 15 MeV bremsstrahlung and 12 MeV monoenergetic gamma sources perform as well as the neutron source in producing a useful fission rate in all threats and are superior in the poly threat. For the bremsstrahlung sources, the magnitude of the fission rate produced is very sensitive to the beam endpoint energy, with the 15 MeV beam producing more than two decades higher fission rates than the 10 MeV bremsstrahlung source. Both the neutron and bemsstrahlung sources impart high radiation doses to the container and its contents

while the monoenergetic photon sources produce approximately an order of magnitude lower dose rate.

TABLE 4. Calculated fission rates for various interrogation sources normalized to an intensity of 10^{10} /s.

Sources scaled to 10^{10} /s	Fission Rate (fissions/s) Bare	Poly Cargo	Iron Cargo
6 MeV mono	4.9E2	5.4E1	1.1E0
12 MeV mono	1.7E4	5.6E3	2.7E3
10 MeV brem	6.4E3	1.0E3	2.8E1
15 MeV brem	1.3E5	3.9E4	1.5E3
D-T neutrons	7.9E5	1.6E3	8.0E5

TABLE 5. Calculated dose rates for various interrogation sources normalized to an intensity of 10^{10} /s.

Sources scaled to 10^{10} /s	Dose Rate (mrem/s)
6 MeV mono	0.13
12 MeV mono	0.21
10 MeV brem	1.44
15 MeV brem	2.84
D-T neutrons	3.48

The source metric, ratio of fissions/mrem, was determined for the three cargo configurations and six interrogation sources (including the D-D neutron source). The results are depicted graphically in Fig. 28. Examination of the fission/mrem ratio shows that neutron sources produce ~10^5 fissions/mrem on the bare and iron threats, but did poorly on the poly cargo. On this metric the difference in performance among the various neutron sources is insignificant. The most challenging case for neutron sources is the poly cargo where only the highest energy sources produced adequate fission. The simulation statistics are poor so the numerical data cannot be considered precise for this threat. Looking at the results for photon interrogation sources we find that bremsstrahlung sources suffer a much larger dose for a given number of fissions than is the case for either neutron sources or monoenergetic photon sources. The bremsstrahlung sources are in a range three decades lower on this metric, i.e. 10^1-10^2 fissions/mrem. The electron endpoint energy is a critical parameter for bremsstrahlung sources with the 15 MeV endpoint systems performing about an order of magnitude better than the 10 MeV endpoint systems. The 15 MeV endpoint energy bremsstrahlung sources perform less well than the neutron sources for all threats except the poly cargo where the bremsstrahlung sources are in the range 10^3-10^4 fission/mrem. The 12 MeV monoenergetic photon source produces fissions/mrem of around 10^4 for all threats, while the 6 MeV source is significantly lower for the iron scenario. For the poly threat that challenges neutron sources, the monoenergetic photon sources do well with fissions/mrem in the range 10^2-10^5, substantially better than the neutron sources and as good as or better than the bremsstrahlung sources. Thus, the superiority of photon sources is clear for the poly threat. In some cases, a weak

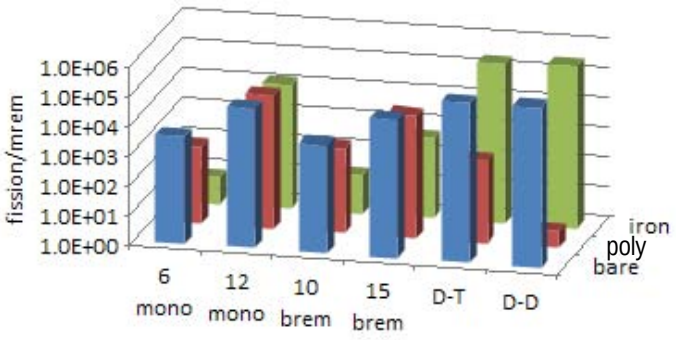

FIGURE 28. Ratios of fissions/mrem for various interrogation sources and shielding configurations.

performance on this metric can be offset by a very robust radiation signature or highly capable detectors that perform very well distinguishing the signature from interferences, so the results in Fig. 28 are only a rough guide. It is also clear that the monoenergetic photon interrogation sources perform well against the largest number of scenarios, but they fail on some threats nonetheless.

The above analysis underestimates actual background variations which could be substantial. A detailed analysis would need to account for specific detectors and the extent to which sources/shields change during a measurement in order to reliably predict actual background variations. The present results are useful only for preliminary guidance and better estimates based on real experience are required as prototypes are taken to the field.

9. SUMMARY

Detecting and characterizing shielded fissionable material is a challenging problem. Conventional passive methods rely on spectroscopy of low-energy (less than 500 keV) gamma-rays from natural decay, but this approach is not suitable when thick shielding is present. For example, the attenuation of 500 keV gamma-rays is such that only about 20% penetrate 2.54 cm of steel (only about 1% penetrate 2.54 cm of lead shielding). There are a number of neutron and photon active interrogation techniques whose sources are predicted to produce adequate numbers of fissions to subsequently produce gamma/neutron signals by both prompt and delayed fission, and providing unique signatures for detecting SNM. Which of these techniques is most efficacious cannot be determined at this point due to insufficient definitions of system design and inadequate data on detector design and interferences. We used the fissions/mrem metric to assess the effectiveness of the interrogation source only and, even in this case, assumptions were made regarding the operational source performance. Our computational analysis found that the differences in the metric between using a D-D versus D-T neutron source are small. The modeling also indicated that bremsstrahlung photon interrogation sources work best on the thick hydrogenous cargos, but carry a significant collateral dose burden. A monoenergetic photon source having energy near the threshold (5.5 MeV) of photofission performs well on thick hydrogeneous cargos similar to the bremsstrahlung sources. However, the monoenergetic photon source imparts approximately an order of magnitude lower dose rate to surroundings compared to a bremsstrahlung source. A monoenergetic photon source having energy near the peak (14 MeV) of the photofission cross section works well over all shielding configurations (constant fissions/mrem metric), and also has about ten times lower imparted dose rate than the bremsstrahlung and neutron sources.

The particular active interrogation source explored in this LDRD is based on using low-energy nuclear reactions to produce neutrons and mono-energetic photons (gammas). The viability of this concept was evaluated through a combination of accelerator-based experiments and computational simulations. Our accomplishments included identifying lanthanum hexaboride (LaB_6) and boron carbide (B_4C) as the leading (p,γ) target materials for a 12-MeV gamma source using the p-^{11}B reaction. For neutron (via d-^{7}Li) or 6-MeV gamma (via p-^{19}F) production, we determined that LiF and CaF_2 are the most promising target materials, but some material issues still need to be resolved. Through ion accelerator experiments, we demonstrated the detection of photofission signatures from depleted uranium and have investigated alternative neutron-producing reactions at low energies. The results from these studies eventually led to the development/testing of a first-generation axial-type gamma tube (funded by DOE/NA-22) and the design/construction of a prototype high power coaxial-type gamma generator (funded by DHS/DNDO). Both of these gamma sources utilized the $^{11}B(p,\gamma)^{12}C$ nuclear reaction to generate 12-MeV gamma beams. The performance of the axial-type gamma tube was evaluated through a series of experiments that measured the gamma intensity as a function of proton energy, beam current, and angle. A gamma yield of 2.0×10^5 was measured with 1 mA of proton beam current on a LaB_6 target at the operating potential of 175 kV. Based on this measurement, the gamma tube is expected to generate 10^6 γ/s with

1 mA of proton current when using a pure ^{11}B target. The angular distribution intensity ratio between 60° and 0° was determined to be 91 ± 0.7% comparing well to previous published results and indicating enhanced gamma directionality in the forward (interrogating) direction. Gamma-ray induced neutrons from depleted uranium and lead were detected in photonuclear experiments with the gamma tube and the results were used to validate MCNPX models.

The above nuclear reaction-based gamma generators are first-generation prototype devices and further research is needed of all technical parameters affecting their output intensities, the interrogation particles and nuclear reactions utilized, and all engineering parameters for attaining high voltage, high intensity sources. The achievable gamma intensity depends on many variables including the employed nuclear reaction, target material, design constraints, power supply, etc. For example, we used the $^{11}B(p,\gamma)$ nuclear reaction in the first-generation generators because 1) it produces 12-MeV monoenergetic gammas for photofission, 2) it is nature's lowest energy nuclear reaction, and 3) the gamma source design could be adapted from existing neutron generators. The main limitation of this reaction is its small gamma production cross section (0.16 mb) at the low-energy resonance (163 kV). Results of accelerator experiments made at low power indicated that the as-configured gamma generators could achieve intensities on the order of 10^8 γ/s. We anticipate that with further design optimization, gamma intensities or approximately 10^9 γ/s could be achieved with the $^{11}B(p,\gamma)$ reaction resonance, but $>10^{10}$ γ/s would present greater technological challenges, including the need to develop advanced compact high voltage power supplies and investigate other mono-energetic gamma-producing nuclear reactions. In regards to the latter approach, the $^{7}Li(d,n\gamma)^{8}Be$ reaction is particularly intriguing for use in compact neutron/gamma generators because a very intense gamma beam can be produced with only modest beam current (~40 mA beam current is needed to generate $>10^{10}$ γ/s with 365 keV deuterons). An intense neutron source could also be developed because of the reaction's large production cross section above 300 keV.

A comprehensive evaluation of the FIND interrogation system requires definition of the system design, data on detector design, and detectable signatures and background interferences. Simulations can identify some of the interferences that reduce detection and increase false alarm, but experience indicates that experimental data obtained with real sources and real detectors is essential to reliable predictions of performance for these techniques. The proposed FIND interrogation system is at a very early stage of development and the needed experimental and simulation data are not available so reliable performance estimates cannot be made yet. A well-focused research program would be beneficial to the extent that it addressed specific and well-posed questions stimulated by the current analysis (e.g., exploration of the concurrent production of multiple modalities via one reaction). A more specific analysis could then be done to indicate reliably the potential performance of the proposed technique. At the same time, combinations of techniques could be applied to a more comprehensive solution to the shielded SNM detection problem.

10. REFERENCES

1. E.T. Kvamme, J.C. Earthman, D.B. Leviton, B.J. Frey, (Proceedings of SPIE: Cryogenic Optical Systems and Instruments XI, J.B. Hearney, L.G. Burriesci, Editors), v. 5904 (2005) 5904N.

2. G. Moebus, J. Tsai, "Nanopatterning and Grain Growth in Fluorides," submitted to Proceedings of Microscopy and Microanalysis 2008.

3. *Materials Safety Data Sheets*, Electronic Space Products International, 1050, Benson Way, Ashland, OR 97520; Product Identification Trade Name: Lithium Oxide.

4. C. Michaelsen, C. Gente, and R. Bormann, J. Mater. Res., Vol. 12, No. 6 (1997) 1463.

5. J. Gillardeau, Y. Macheteau, P. Plurien, and J. Oudar, Oxidation of Metals, Vol. 2, No. 3 (1970).

6. V.Y. Yakovlev, E.V. Kabanova, T. Weber, P. Paufler, Physics of the Solid State, Vol. 43, No. 8 (2001) 1580-1584.

7. http://www.srim.org/

8. L.C. Feldman and S.T. Picraux, in *Ion Beam Handbook for Material Analysis*, (J.W. Mayer and E. Rimini, eds.), Academic Press, Inc., New York, NY (1977).

9. T. Gozani, Nucl. Instrum. Meth. A **353** (1994) 635.

10. M.L. Firouzbakht, D.J. Schlyer and A.P. Wolf, Nucl. Med. Biol. 25 (1998) 161.

11. Ibid. 8

12. R.W. Michelmann, J. Krauskopf and K. Bethge, Nucl. Instrum. Meth. B **51** (1990) 1.

13. K. Von Wohlleben and E. Schuster, Radiochim. Acta **12** (1969) 75.

14. B.J. Guzhovskij, S.N. Abramovich and V.A. Pereshivkin, Vop. At. Nauki i Tekhn. **2** (1984) 55.

15. B. Anders, P. Herges and W. Scobel, Z. Phys. A **301** (1981) 353.

16. F. Ajzenberg-Selove, Nucl. Phys. **A506** (1990) 1.

17. D. Tilley *et al.*, Nucl. Phys. **A745** (2004) 155.

18. Arizona Carbon Foil Co., Tucson, AZ.

19. D.R. Lide, ed., *CRC Handbook of Chemistry and Physics*, Vol. 87 (The Chemical Rubber Co., Cleveland, OH, 2006), 87th Edition.

20. G. Dietz and H. Klein, *NRESP4 and NEFF4 Monte Carlo Codes for the Calculation of Neutron Response Function and Detection Efficiencies for NE 213 Scintillation Detectors* (Physikalisch-Technische Bundesanstalt, Bundesalle 100, W-3300 Braunschweig, 1982).

21. D.E. Gonzalez Trotter, Ph.D. Thesis, Duke University (1997).

22. F. Salinas Meneses, Ph.D. Thesis, Duke University (1998).

23. A. Sabourev *et al.*, Phys. Rev. C **73** (2006) 015801.

24. J. Verbeke, A.S. Chen, J. L. Vujic, and K.N. Leung, Nucl. Tech. 134 (2001) 278; J. Verbeke, J. L. Vujic, and K.N. Leung, Nucl. Tech. **129** (2000) 257.

25. G.L. Jenkins, L.W. Cochran, *et al.*, Phys. Rev. 91(4) (1953) 915.

26. D. Slaughter *et al.*, LLNL Report UCRL-ID-155315 (2003).

27. G. R. Keepin, LANL Report LA-4457-MS (1970).

28. J.L. Jones *et al.*, Nucl. Instr. Meth. **B241** (2005) 770.

29. J.L. Jones *et al.*, Application of Accelerators in Research and Industry: 17th Int'l. Conference (J.L. Duggan and I.L. Morgan, editors) AIP Conference Proceedings, Vol. 680, Melville, New York (2003) 947.

30. C.E. Moss, C.A. Goulding, C.L. Hollas, and W.L. Myers, Application of Accelerators in Research and Industry: 17th Int'l. Conference (J.L. Duggan and I.L. Morgan, editors) AIP Conference Proceedings, Vol. 680, Melville, New York (2003) 900.

Distribution

1	MS0484	Russell Skocypec	08004
1	MS0484	James Riley	10542
1	MS1056	Barney Doyle	01111
1	MS1056	Floyd McDaniel	01111
1	MS1415	David Sandison	01100
1	MS1415	Paolo Rossi	01111
1	MS1421	Paula Provencio	01111
1	MS1427	Julia Phillips	01100
1	MS9004	Jill Hruby	08100
1	MS9004	William Ballard	08100
1	MS9004	Patricia Falcone	08110
1	MS9004	Duane Lindner	08120
1	MS9004	Brian Damkroger	08130
1	MS9290	James Wilhelm	08529
1	MS9292	Thomas Raber	08131
5	MS9402	Arlyn Antolak	08131
1	MS9402	John Goldsmith	08131
1	MS9402	Kristin Hertz	08131
1	MS9402	Daniel Morse	08131
1	MS9406	James Lund	08132
1	MS9671	Michael King	08131
2	MS9018	Central Technical Files	08944
2	MS0899	Technical Library	04536
1	MS0123	D. Chavez, LDRD Office	01011


Sandia National Laboratories